**ROYAL
AERONAUTICAL
SOCIETY**

REGULAR PAPER

Multi-fidelity and multi-objective aerodynamic short nacelle shape optimisation under different flight conditions

G.C. Tao[1,2] , W. Wang[1,2], Z.T. Ye[2], Y.N. Wang[1,2], J.Q. Luo[1] and J.H. Cui[1,2]

[1]Department of Aeronautics and Astronautics, Zhejiang University, Hangzhou, China and [2]ZJUI Institute, Zhejiang University, Haining, China
Corresponding author: J.H. Cui; Email: jiahuan.cui@zju.edu.cn

Abstract

Throughout the course of a flight mission, a range of aerodynamic conditions, including design-point conditions and off-design conditions, are encountered. As the bypass ratio increases and the fan-pressure ratio decreases to reduce the engine's specific fuel consumption, the engine diameters increase, which results in an increase in the nacelle weight and overall drag. To reduce its weight and drag, a shorter nacelle with a length-to-diameter ratio $L/D = 0.35$ is investigated. In this study, an adaptive cokriging-based multi-objective optimisation method is applied to the design of a short aero-engine nacelle. Two nacelle performance metrics were employed as the objective functions for the optimisation routine. The cruise drag coefficient is evaluated under cruise conditions, whereas the intake pressure recovery is evaluated under takeoff conditions. The cokriging metamodel are refined using an effective infilling strategy, where high-fidelity samples are infilled via the modified Pareto fitness, and low-fidelity samples are infilled via the Pareto front. By combining parameterised geometry generation, automated mesh generation, numerical simulations, surrogate model construction, Pareto front exploration based on the non-dominated sorting genetic algorithm-II and sample infilling, an integrated multi-objective optimisation framework for short aero-engine nacelles is developed. Two-objective and three-objective test functions are used to validate the effectiveness of the proposed framework. After the optimisation process, a set of non-dominated nacelle designs is obtained with better aerodynamic performance than the original design, demonstrating the effectiveness of the optimisation framework. Compared with the kriging-based optimisation framework, the cokriging-based optimisation framework outperforms the single-fidelity method with a higher hypervolume value at the same number of iteration loops.

Nomenclature

a	number of nodes in the boundary layer normal to the wall
A	Bernstein polynomial weighting coefficients
A_{hi}	highlight area, m²
b	average spacing on the fancowl surface in the axial direction
BP	Bernstein polynomial
c	number of nodes in the circumferential direction
$\mathbf{c}$	a column vector of the covariance of $\mathbf{X}$
C	class function
$\mathbf{C}$	covariance matrix
$\widetilde{C}$	covariance matrix of augmented dataset
$C_{D-\text{cruise}}$	ratio of the drag force at the fancowl to the force produced by the dynamic pressure multiplied by the area at highlight
C_{fx}	skin-friction coefficient along the wing sections

d	number of nodes in the radial direction
$\mathbf{d}$	difference in trends between the low-fidelity and high-fidelity data
distance	distance criterion
D_{nac}	drag force at the fancowl
e	number of nodes from the nacelle to the farfield
f_i	location of the intake throat (fraction of intake length)
f_{max}	location of the maximum radius (fraction of nacelle length)
f_{sk}^i	normalised k-th objective function at the i-th sampling point
G_i	Pareto fitness at the i-th sampling point
IPR_{takeoff}	ratio of the total pressure at the fanface to the total pressure of the freestream at takeoff condition
k	number of design variables
K	binomial coefficient
l_{nac}	nacelle length, m
M_∞	freestream Mach number
MG_i	modified Pareto fitness at the i-th sampling point
MLE	maximum likelihood estimation
N_1, N_2	class function leading-edge and trailing-edge parametres
n_{hi}	number of high-fidelity samples
n_{lo}	number of low-fidelity samples
p_j	correlation parametre
P_{st}	freestream static pressure, Pa
P_{t}	inlet total pressure, Pa
P_0	freestream total pressure, Pa
$\bar{P}_{0,fanface}$	mean total pressure at the fanface, Pa
ρ	scaling factor
r_i	intake throat radius, m
r_{if}	initial forebody radius of curvature, m
r_{fan}	radius of fan, m
r_{hi}	radius of highlight, m
r_{max}	maximum radius of the fancowl, m
r_{te}	radius of trailing-edge, m
S	shape function
T_{st}	Freestream static temperature, K
T_{t}	inlet total temperature, K
V_∞	freestream air speed, m/s
$x_j^{(i)}$	j-th design variable of i-th sample
$\mathbf{x}$	predicted sample location
$\mathbf{X}$	samples locations
$\mathbf{X}_{\mathrm{hi}}$	high-fidelity sample locations
$\mathbf{X}_{\mathrm{lo}}$	low-fidelity sample locations
$\widetilde{X}$	argumented dataset by argumenting the observed data with the predicted data
X_k	sample set of the k-th cluster
$\chi_{infill}^{(k)}$	selected high-fidelity infill samples
y_1^+	first cell y-plus
$\hat{y}_{\mathrm{hi}}(\mathbf{x})$	maximum likelihood estimates for the predicted data
$\tilde{\mathbf{y}}$	values at $\widetilde{\mathbf{X}}$
$\mathbf{Y}$	values at sample locations
$\mathbf{Y}_{\mathrm{lo}}(\mathbf{X}_{\mathrm{lo}})$	values at low-fidelity sample locations
$\mathbf{Y}_{\mathrm{hi}}(\mathbf{X}_{\mathrm{hi}})$	values at high-fidelity sample locations
$Z_{\mathrm{d}}(.)$	difference between $Z_{\mathrm{lo}}(.)$ and $Z_{\mathrm{hi}}(.)$
$Z_{\mathrm{hi}}(.)$	gaussian process of high-fiedlity simulations
$Z_{\mathrm{lo}}(.)$	gaussian process of low-fiedlity simulations
CRM	common research model
ACARE	Advisory Council for Aviation Research and Innovation in Europe
NLF	natural laminar flow
CFD	computational fluid dynamics

LHS	Latin hypercube sampling
CST	class/shape transformation
iCST	intuitive class/shape transformation
IGD	inverted generational distance
HV	hypervolume
IPR	intake pressure recovery

Greek Symbol

ρ_∞	freestream air density, kg/m^3
η	non-dimensional span station(0 = root, 1 = tip)
ζ	non-dimensional aerofoil abscissa, y/c
ψ	non-dimensional aerofoil ordinate, x/c
θ_j	correlation coefficient of j-th design variable
θ_{lo}	correlation parametre
θ_d	correlation parametre
$\hat{\boldsymbol{\theta}}_d$	maximum likelihood estimates for θ_d
σ_d	standard deviation of $Z_d(.)$
σ_{lo}	standard deviation of $Z_{lo}(.)$
$\hat{\sigma}_d$	maximum likelihood estimates for σ_d
$\hat{\sigma}_{lo}$	maximum likelihood estimates for σ_{lo}
ψ_d	correlation in $Z_d(.)$
ψ_{lo}	correlation in $Z_{lo}(.)$
Ψ_d	matrix of correlations of the form ψ_d
Ψ_{lo}	matrix of correlations of the form ψ_{lo}
Φ	circumferential angle
β_{nac}	boat-tail angle
$\hat{\mu}$	maximum likelihood estimates for mean of $\widetilde{y}$
$\hat{\mu}_d$	maximum likelihood estimates for the mean of $\mathbf{d}$

1.0 Introduction

Engine nacelle is a key component of an aircraft and typically consists of an inlet cowl, a fancowl, a thrust reverser, a core cowl and a primary exhaust nozzle. It plays an important role in the flight mission to provide smooth aerodynamic fairing for internal core components while ensuring a smooth airflow into the engine [1]. The aerodynamic shape optimisation of an engine nacelle is complicated. The configuration is non-axisymmetrically controlled using relatively large design variables. In addition, an entire flight mission includes different operating conditions, such as takeoff, crosswind and cruise. If all these conditions are to be addressed, multi-objective optimisation must be used, which inevitably increases the complexity of the optimisation process.

The design requirements for engine nacelles continue to change. The Advisory Council for Aviation Research and Innovation in Europe (ACARE) proposed the goal of flight path 2050 to reduce CO_2 and NO_x emissions by 75% and 90% per passenger kilometer, respectively, compared to a typical new aircraft in 2000 [2]. As for civil aero-engines, to achieve these goals, the bypass ratio is increasing [3] by lowering the fan-pressure ratio [4]. Consequently, the fan diameter must be increased to allow more mass flow through the fan to generate a similar level of thrust. As the nacelle size increases, so does the associated drag and weight [5]. Therefore, advanced nacelle designs with shorter inlets and exhaust nozzles are required to ensure that the achieved performance benefits are not outweighed by the increased installation drag and propulsion-system weight [6–8].

Over the past 20 years, surrogate-based aerodynamic shape optimisation of engine nacelles has been conducted for various objectives. Song and Keane [9] built a surrogate model using kriging to find better designs with higher pressure recovery and larger scarf angles for a three-dimensional (3D) subsonic civil engine nacelle. Fang et al. [10] developed a platform for optimising a 3D powered-on nacelle of a transonic civil aircraft to minimise drag and increase internal volume. Nacelle optimisation has been

obtained through hybrid methods that combine the non-dominated sorting genetic algorithm-II (NSGA-II) and kriging models. Zhong and Li [11] developed a 3D shape design and optimisation method for natural laminar flow (NLF) nacelles to minimise frictional drag. The procedure starts with two-dimensional (2D) optimisation of the profile to narrow down the design space for 3D optimisation. This is followed by building a kriging surrogate model and adopting an adaptive simulated annealing algorithm to find the best design. Yao et al. [12] established an adaptive-surrogate-based robust optimisation strategy for NLF nacelles to increase the favourable pressure gradient region and volume ratio of the nacelle by increasing its lip radius and reducing its maximum diameter.

To better investigate the performance of the engine nacelle during the cruise condition, except for the cruise drag, typically the spillage drag (CD-spill) and the drag rise Mach number (MDR) are considered [13–18]. Robinson et al. [13] demonstrated a multi-objective optimisation method using an evolutionary genetic algorithm and applied it to aerodynamic shape optimisation in a 2D axisymmetric nacelle to study its performance under different conditions. Kriging was used as the RSM interpolation tool, and NSGA-II was adopted to explore the 3D Pareto surfaces. Tejero et al. [18] presented an adapted method whose main principle is that, as the genetic algorithm progresses through generations, the optimisation focuses on narrower parts of the design space where the optimal designs are likely to be located to improve the prediction accuracy. Surrogate models have been constructed using the kriging interpolation methods, and NSGA-II has been used to explore the Pareto surfaces. In addition to the three objectives mentioned above, Schreiner et al. [19] considered two off-design windmilling conditions to extend the approach to account for off-design conditions. These are the cruise engine-out conditions (CD-windmill) and diversion conditions (CD-diversion).

To date, few studies have focused on the optimisation of short nacelles. Cipriani [20] constructed an optimisation framework based on kriging as a surrogate model and investigated the effects of the geometrical parametres of the short-intake bottom line on the aerodynamic behaviour at the fanface under takeoff conditions. Sanchez Moreno et al. [21] proposed a method for compact and aerodynamically robust nacelle optimisation using a single-fidelity surrogate modeling approach based on Euler computations, whereas kriging interpolation and artificial neural networks are used for low-order models.

As discussed above, surrogate models are built only on high-fidelity data. Recently, there has been a trend to blend low-fidelity data with high-fidelity data to further improve prediction accuracy [22]. Cokriging [23] was proposed by Kennedy and O'Hagan by blending the information from high-fidelity data and low-fidelity data. This has been widely used in aerodynamic optimisation problems. Toal and Keane [24] showed that cokriging is as effective as that produced using a traditional multipoint process when optimising a transonic aerofoil but with a reduction in the total number of computational fluid dynamics (CFD) simulations. Priyanka et al. [25] carried out aerodynamic shape optimisation of an aerofoil using cokriging and obtained 18.08% and 38.70% improvements for maximising C_l and $C_l^{3/2}/C_d$, respectively, compared with the baseline NACA0012 aerofoil. Tejero et al. [26] optimised an installed aero-engine short nacelle using cokriging and obtained a new configuration with an increment of 0.65% in the net vehicle force. However, there is no open literature on multi-objective optimisation of short nacelles based on a multi-fidelity surrogate model.

In this study, a short nacelle with a length-to-diameter ratio $L/D = 0.35$ was selected as the design object. A cokriging model was adopted as the surrogate model. Takeoff and cruise conditions were considered in the optimisation process to determine the optimal design. The remainder of this paper is organised as follows. In Section 2.0, the individual modules within the optimisation framework are described in detail and the proposed optimisation framework is validated using two test functions. Section 3.0 presents the results and discussion of the aerodynamic shape optimisation of a non-axisymmetric nacelle. Finally, Section 4.0 presents the conclusions.

2.0 Methodology

An integrated adaptive cokriging-based multi-objective optimisation framework was applied in this study, denoted as MO-ACK [27]. A flowchart of the MO-ACK is shown in Fig. 1. The framework
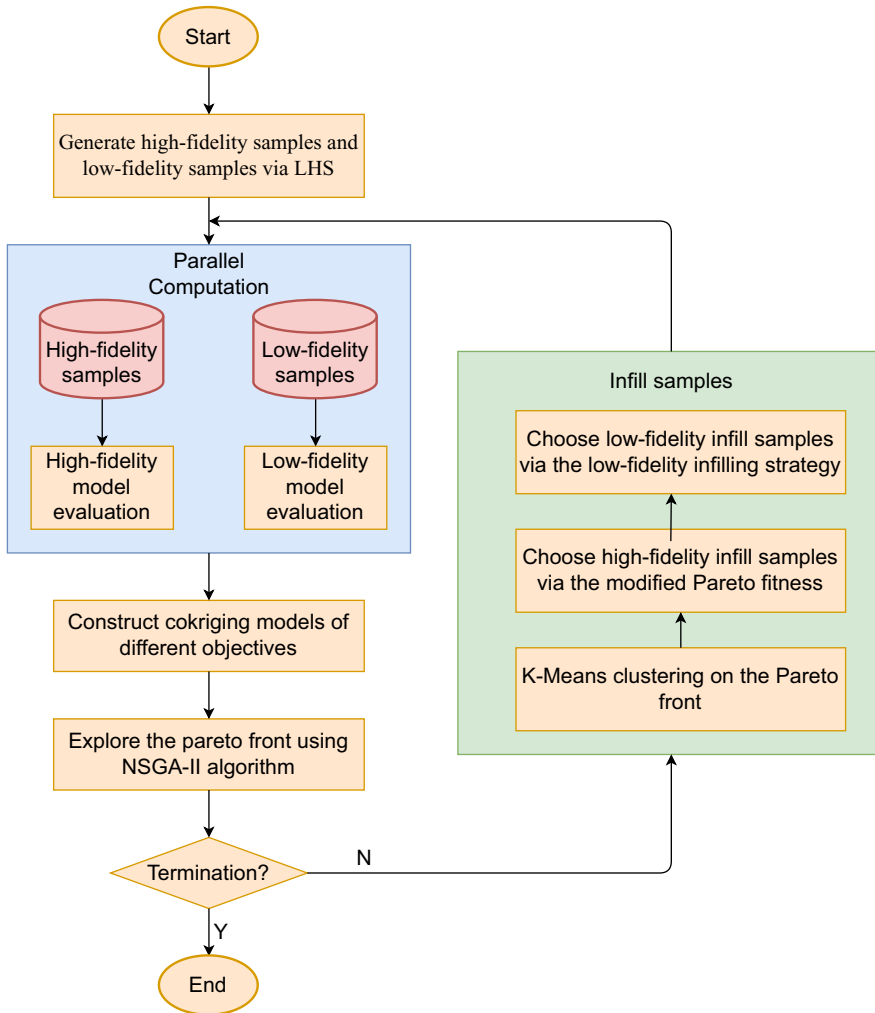
Figure 1. *Flowchart of the MO-ACK optimisation framework.*

comprised several fundamental modules, including sampling methods, parametric geometry defini-
tion, automatic mesh generation, performance computation of nacelle designs, surrogate models,
optimisation algorithms and infilling methods.

The optimisation routine was initialised using nested Latin hypercube sampling (LHS) to create the
initial samples. Such designs are useful for conducting multiple simulation experiments with varying
levels of accuracy [28]. Subsequently, initial samples of different levels of accuracy were evaluated in
parallel by means of CFD to obtain the data of interest, which was used as the input transferred to the
surrogate model. Generally, there are more samples with low-level accuracy than those with high-level
accuracy, because the calculation time of a single sample with low-level accuracy is shorter than that
with high-level accuracy. Consequently, the computational time spent on high-level accuracy samples is
at the same level. The cokriging model was then used as a surrogate model to predict objective values.
It can effectively blend two sets of data to achieve a higher prediction accuracy. The NSGA-II [29]
was driven by the trained surrogate model during the optimisation step to explore the Pareto front. After
each optimisation step, the sample dataset was updated by infilling the new samples until the termination
condition was achieved. The details of these modules are described below.

2.1 Geometry definition

Kulfan [30, 31] proposed a unique and powerful geometry representation method called class/shape transformation (CST). The analytical CST geometry representation methodology provides a unified and systematic approach to present a wide variety of 2D and 3D geometries, encompassing a significantly large design space with relatively few parametres. Zhu and Qin [32] extended the CST method and proposed a new aerofoil parameterisation method called intuitive class/shape transformation (iCST), which combines the flexibility and accuracy of the CST method with the intuitiveness of the PARSEC method. Christie et al. [33] developed a system that analytically calculates the transformation matrix for a set of geometric constraints based on the iCST method and successfully applied it to construct a 3D axisymmetric nacelle. The iCST method has been successfully applied to parameterise various aerodynamic shape optimisation problems [34].

In this study, the iCST method was applied to parameterise the surface of the fan cowl and intake. This method consists of shape and class functions. The class function is used to define the general classes of geometry, whereas the shape function is used to define specific shapes within the geometry class. The general mathematical expression of CST is of the following form:

$$\zeta(\psi) = C_{N_2}^{N_1}(\psi)\, S(\psi) + \psi\, \Delta\zeta_{TE}; \quad \zeta = \frac{z}{c}; \quad \psi = \frac{x}{c} \tag{1}$$

where $C_{N_2}^{N_1}$ is the class function, $S(\psi)$ is the shape function, and $\psi\,\Delta\zeta_{TE}$ controls the trailing-edge thickness. The mathematical expression of the class function is of the following form:

$$C_{N_2}^{N_1}(\psi) = \psi^{N_1}(1 - \psi)^{N_2} \tag{2}$$

where N_1 and N_2 are tuned to obtain different shapes, as shown in Fig. 2. For a round-nose aerofoil, usually $N_1 = 0.5$ and $N_2 = 1.0$.

The shape function was constructed using a Bernstein polynomial with different weight coefficients. The mathematical expression of the Bernstein polynomials is

$$BP(\psi) = \sum_{i=0}^{N} \left[K_{i,N} \cdot \left(\psi^i \cdot (1 - \psi)^{N-i} \right) \right]; K_{i,N} = \frac{N!}{i!(N-i)!} \tag{3}$$

In addition, the shape function used in this study can be expressed as

$$S(\psi) = \sum_{i=0}^{N} \left[A_i \cdot K_{i,N} \cdot \left(\psi^i \cdot (1 - \psi)^{N-i} \right) \right] \tag{4}$$

In this work, the open source common research model (CRM) was used and was modified based on the fan diameter to meet the short nacelle $L/D = 0.35$ requirement. The target geometry can be obtained using appropriate weight coefficients. For an axisymmetric nacelle geometry, the aero-lines of the fancowl and intake were first created using the iCST method and then revolved to construct the surface. The aero-lines of the fancowl and intake were defined by several variables, as shown in Fig. 3. To simplify the optimisation process and comply with the specific design requirements, six design variables ($r_{if}, r_{max}, f_{max}, \beta_{nac}, r_i,$ and f_i) were chosen to parameterise a single aero-line, whereas the remaining parametres were set as constants during the optimisation process. As shown in Fig. 3, r_{if} denotes the initial forebody radius of curvature, r_{max} denotes the maximum radius of the fancowl, f_{max} denotes the location of the maximum radius, expressed as a fraction, β_{nac} represents the boat-tail angle, r_i denotes the intake throat radius, and f_i denotes the location of the intake throat, which is expressed as a fraction. The size of the fan and the specific engine limit some of the parametres to being constant. Specifically, when designing an engine nacelle, the $r_{fan}, r_{hi}, r_{te}, l_{nac}$ and l_{int} should match the size of the engine because the aerodynamic shape optimisation of the nacelle is usually performed after the design of the engine. The non-asymmetry of the nacelle was achieved based on three different aero-lines at $\Phi = 0°$, $\Phi = 90°$, and $\Phi = 180°$, as shown in Fig. 4, with $\Phi = 0°$ being the top aero-line of the nacelle. It is worth mentioning that the aero-lines at $\Phi = 90°$ and $\Phi = 270°$ were the same, owing to the left-right symmetry.

(a)

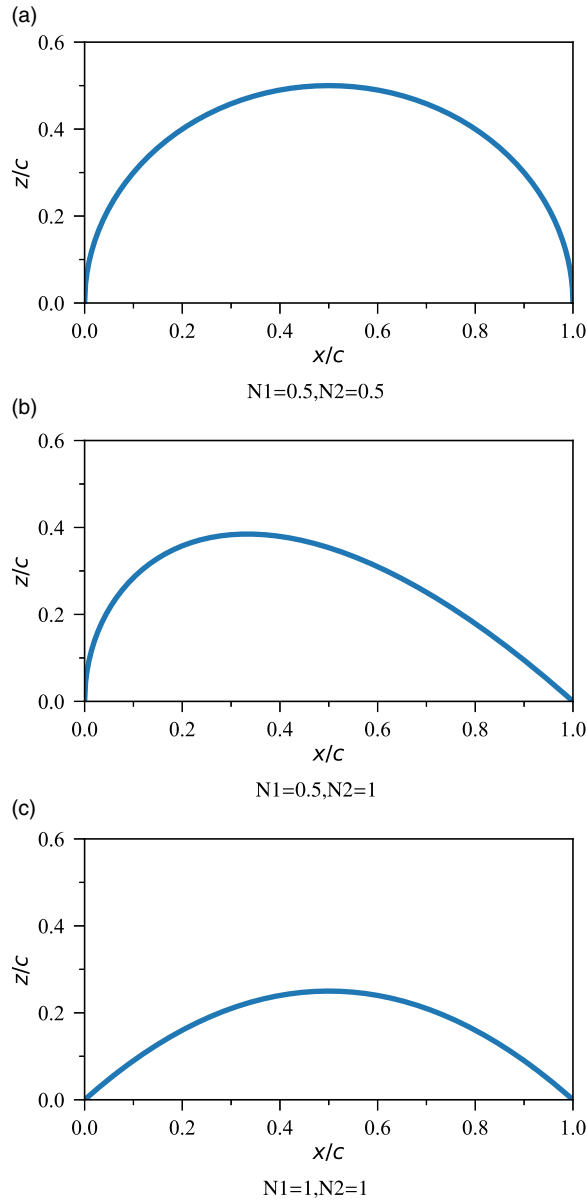N1=0.5,N2=0.5

(b)

N1=0.5,N2=1

(c)

N1=1,N2=1

Figure 2. *Illustration of the effects of N_1 and N_2 on the class function.*
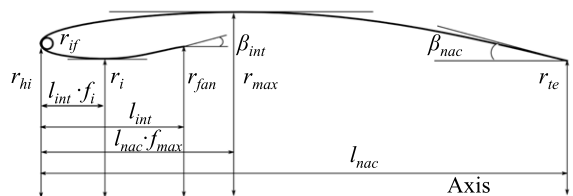
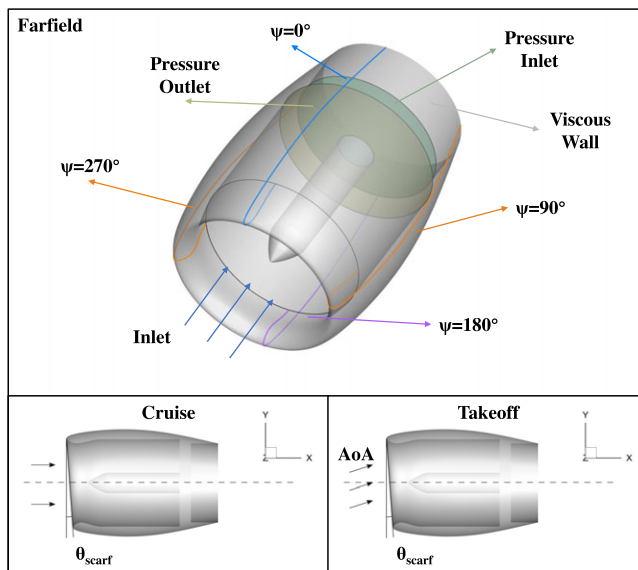**Figure 3.** *Design variables of aero-lines.*

Figure 4. *Schematic of the boundary conditions.*

2.2 Computational method

In this study, the numerical simulations were performed using an in-house CFD solver. The finite-volume method was applied to discretise the governing equations. The implicit Gauss–Seidel method was employed for the time discretisation. Scalar dissipation coupled with the central difference was used to discretise the spatial derivative. The shear stress transport (SST) k-w turbulence model was adopted to close the Reynolds-averaged Navier–Stokes (RANS) equation. Ideal compressible air was assumed for all the simulations. The freestream condition was specified using a pressure farfield boundary condition by setting the static pressure P_{st}, static temperature T_{st}, and Mach number M_{∞}. The takeoff and cruise flight conditions were considered in this study. The exit-pressure boundary condition was applied at the duct ends, extended by 1.8 fan radii downstream of the fan location. It's understood that fan has a significant effect on the flow around with the inlet, especially under the high angle-of-attack. Usually, the presence of fan will improve the performance of nacelle inlet under the large angle. Hence, the current optimisation framework of short nacelle will provide a conservative design. In the future, a fan model will be implemented to improve the optimisation framework for short nacelle. The inlet conditions for the bypass ducts were determined by using P_t and T_t.

To verify the accuracy and validity of the in-house solver, two cases were used as test cases: one was the ONERA M6 wing [35] and the other was the NACA-1-Series inlets [36]. A description of the ONERA-M6 case is presented in Table 1. The surface pressure coefficients calculated using the in-house solver are shown in Fig. 5 and were compared with the data calculated using the FUN3D solver [37–39] and the experimental data. Here, η refers to the span station (0 = root; 1 = tip), and the x-location was non-dimensionalised by the local chord. The skin friction coefficient calculated using the in-house solver is shown in Fig. 6 for comparison with the data calculated using the FUN3D solver. Evidently, in both figures, the results calculated using the in-house solver show good agreement with the FUN3D results. Moreover, in Fig. 5, the in-house solver performs even better than the FUN3D solver when $\eta = 0.44$ and $\eta = 0.65$, and the in-house pressure coefficient distribution is smoother when $x/c = 0.56$ and $x/c = 0.48$ than the FUN3D pressure coefficient distribution.

An axisymmetric NACA 1-85-43.9, with a contraction ratio of 1.250, was adopted as the second test case. Examples of the computed wall-pressure coefficient C_p distribution along the chord normalised abscissa x/c are shown in Fig. 7 for four Mach numbers and mass flow capture ratios (MFCRs) [40].

Table 1. *ONERA M6 case description*

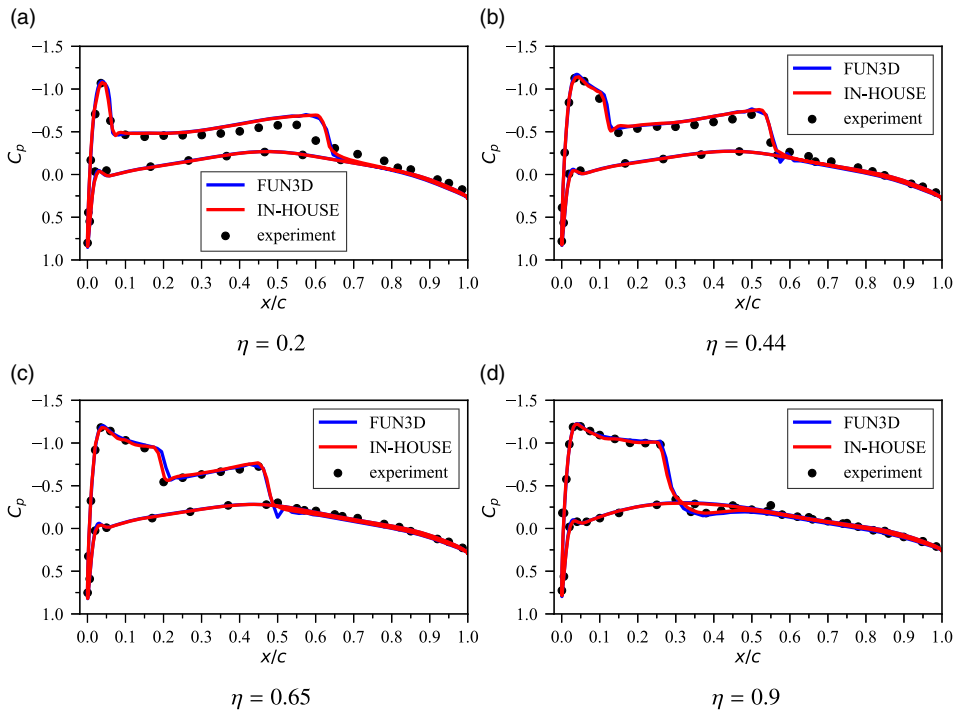| Parametres	Values
Reynolds number based on root chord	14.6×10^6
Freestream Mach number	0.84
Freestream temperature	540R
Angle-of-attack	3.06

Figure 5. *Comparisons of surface-pressure coefficients along the wing sections.*

Evidently, in all four different boundary conditions, the results calculated using the in-house solver show good agreement with the experimental results. The above results show that the in-house solver is suitable for the subsequent optimisation procedures.

To mesh the 3D non-axisymmetric nacelle, ANSYS ICEM was used to create a structured mesh for the computational domain. The first cell height was set to achieve $y_1^+ \approx 1$ with a stretching ratio of 1.2. The mesh details are shown in Fig. 8. As shown in Fig. 9, there are five main parametres for controlling grid variation. The first parametre a indicates the number of nodes in the boundary layer normal to the wall. The second parametre, b, indicates the average spacing on the fancowl surface in the axial direction, which also influences the inner surface grid distribution owing to the structured block. The number of nodes in the circumferential and radial directions was determined using the third parametre c and fourth parametre d, respectively. The number of nodes from the nacelle to the farfield was determined using the fifth parametre, e. The other parametres remained unchanged. Table 2 summarises these parametres. Tables 3 and 4 summarises the boundary conditions used in this study. A mesh-independence study was performed for three different mesh sizes (3.9 M, 8.67 M, and 15.8 M), as shown in Fig. 10. It can be observed that the drag coefficient at cruise condition and pressure recovery at takeoff condition reached the grid convergence at a mesh size of 8.67 M. Therefore, this mesh size was adopted for the following high-fidelity CFD simulation, whereas the mesh size of 3.9 M was adopted for the low-fidelity CFD simulation.
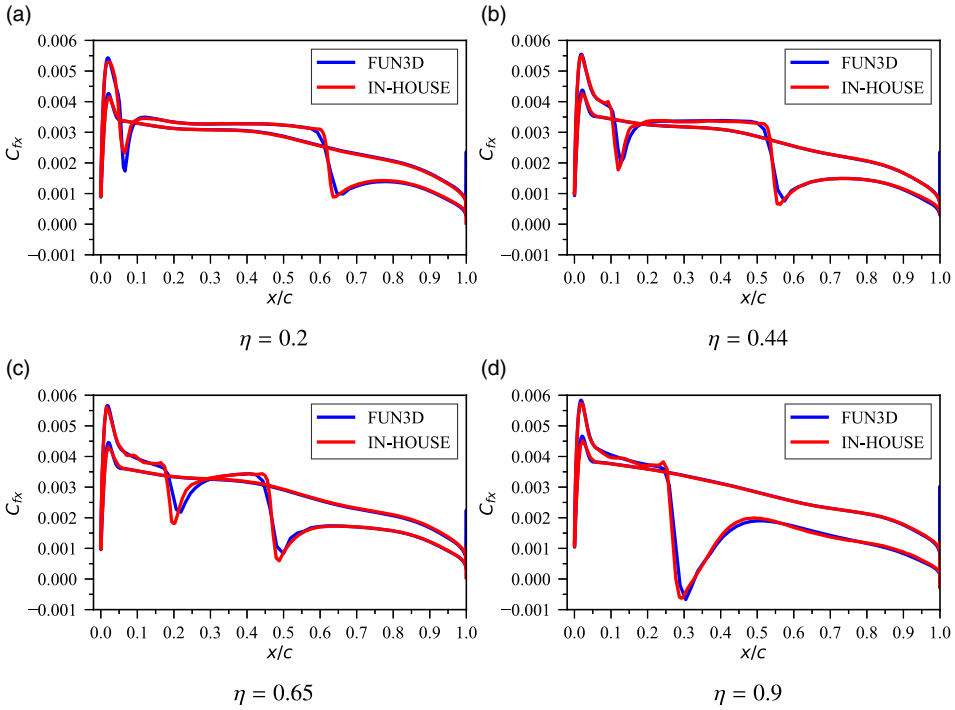
Figure 6. *Comparisons of skin-friction coefficients along the wing sections with results from FUN3D.*
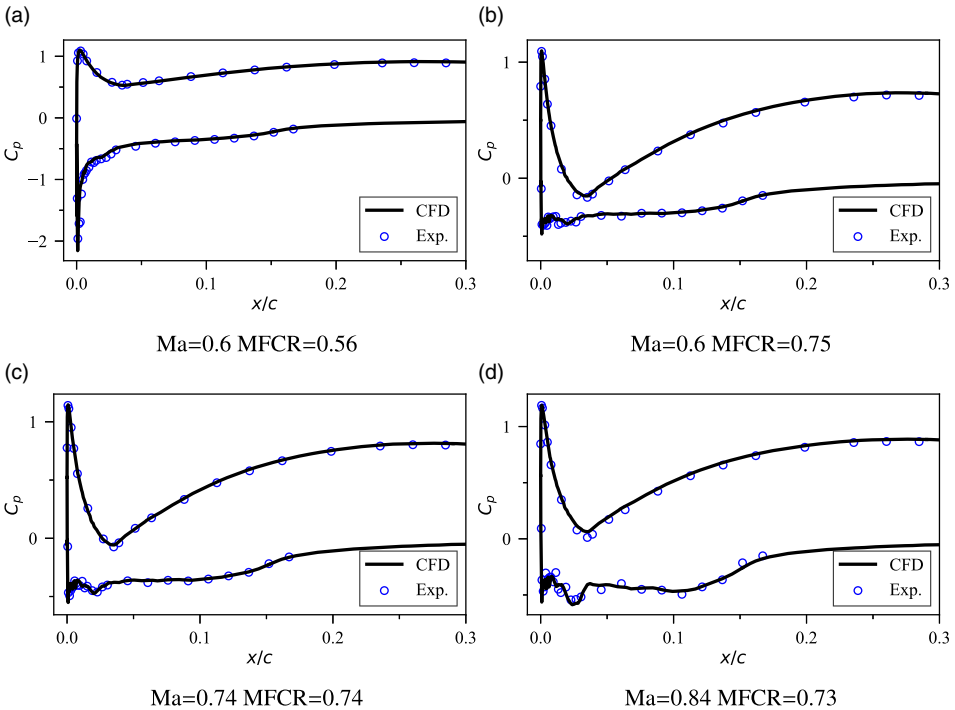

Figure 7. *Comparisons of wall-pressure coefficients on the inlet forebody exterior and lip over a range of mass-flow ratios.*
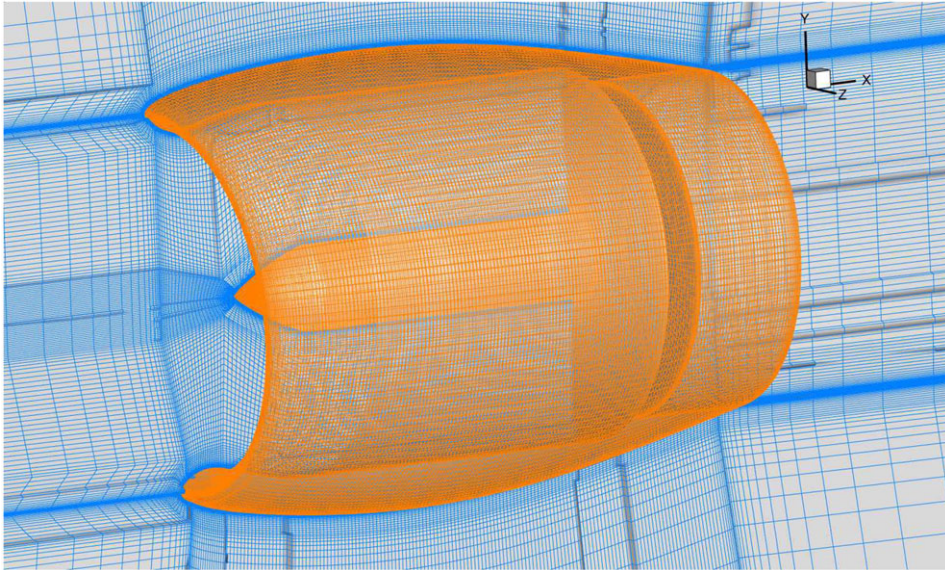
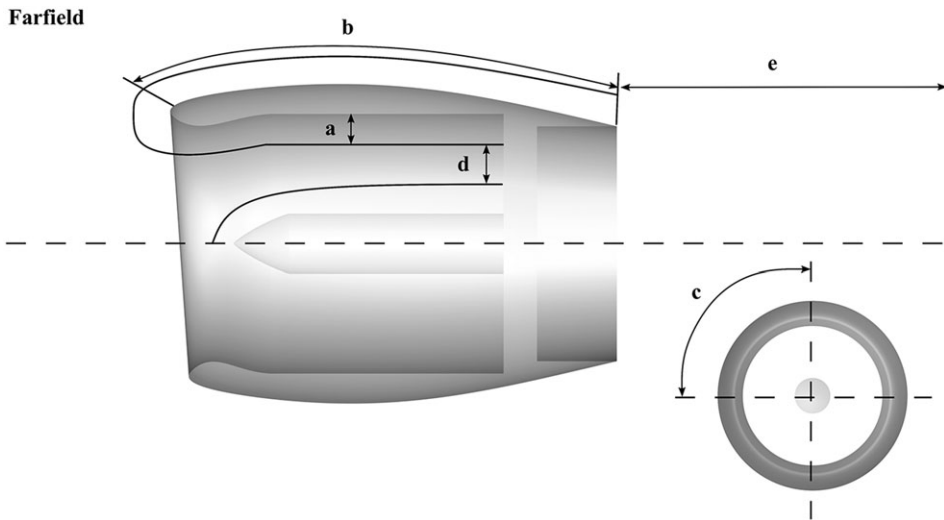**Figure 8.** *Mesh details of the nacelle surface and symmetry plane.*

Figure 9. *Illustration of grid independence varying parametres.*

2.3 Multi-fidelity analysis

In engineering optimisation problems, high-fidelity samples are often difficult to obtain, whereas low-fidelity samples are easier to obtain. With the help of low-fidelity samples, the prediction accuracy of the surrogate model was improved. To make good use of the low-fidelity samples, multi-fidelity analysis was performed, and a multi-fidelity surrogate model was constructed. In this study, cokriging was adopted as the metamodel in the optimisation process. The mathematical formula for cokriging is detailed below.

Table 2. *Parametres in grid independence*

Grid Number (10^6)	a	b	c	d	e
3.9	50	0.06	14	20	35
8.67	50	0.035	21	30	39
15.8	50	0.025	28	40	43

Table 3. *Cruise boundary conditions*

Parametres	Values
Mach number	0.85
Altitude	35000ft
Angle-of-attack	0
Freestream temperature	219K
Outlet static pressure	29kPa

Table 4. *Takeoff boundary conditions*

Parametres	Values
Mach number	0.25
Altitude	Sea level
Angle-of-attack	18°
Freestream temperature	293K
Outlet static pressure	87.7kPa
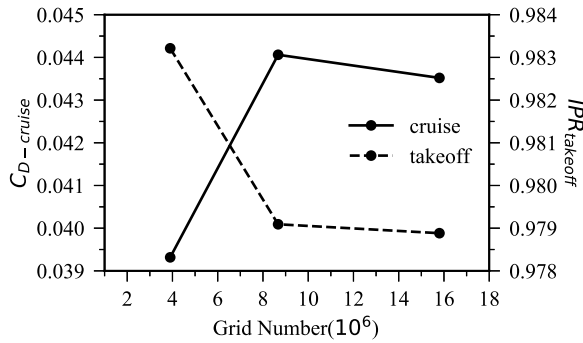
Figure 10. *Grid-independence study results showing the cruse and takeoff condition.*

The samples used in cokriging are expressed using Equation (5), which consists of low- and high-fidelity samples.

$$\mathbf{X} = \begin{pmatrix} \mathbf{X}_{lo} \\ \mathbf{X}_{hi} \end{pmatrix} = \left(\mathbf{x}_{lo}^{(1)} \cdots \mathbf{x}_{lo}^{(n_{lo})} \mathbf{x}_{hi}^{(1)} \cdots \mathbf{x}_{hi}^{(n_{hi})} \right)^{T} \tag{5}$$

where $\mathbf{X}_{lo}$ denotes the low-fidelity sample locations, $\mathbf{X}_{hi}$ denotes the high-fidelity sample locations, and the high-fidelity sample locations coincided with a subset of the low-fidelity sample locations $\mathbf{X}_{hi} \subset \mathbf{X}_{lo}$. In addition, n_{lo} represents the number of low-fidelity samples and n_{hi} represents the number of high-fidelity samples. The value at $\mathbf{X}$ was treated as if it were a realisation of a stochastic process.

$$\mathbf{Y} = \begin{pmatrix} \mathbf{Y}_{lo}(\mathbf{X}_{lo}) \\ \mathbf{Y}_{hi}(\mathbf{X}_{hi}) \end{pmatrix} = \left(\mathbf{Y}_{lo}\big(\mathbf{X}_{lo}^{(1)}\big) \cdots \mathbf{Y}_{lo}\big(\mathbf{X}_{lo}^{(n_{lo})}\big) \, \mathbf{Y}_{hi}\big(\mathbf{X}_{hi}^{(1)}\big) \cdots \mathbf{Y}_{hi}\big(\mathbf{X}_{hi}^{(n_{hi})}\big) \right)^{\mathrm{T}} \tag{6}$$

The local features of the low-fidelity and high-fidelity simulations were represented as the Gaussian process $Z_{lo}(.)$. and $Z_{hi}(.)$. Based on the auto-regressive model, the high-fidelity simulation was approximated as a low-fidelity simulation multiplied by a scaling factor ρ plus a Gaussian process $Z_d(.)$, which represented the difference between $\rho Z_{lo}(.)$ and $Z_{hi}(.)$. The approximation is expressed as

$$Z_{hi}(\mathbf{x}) = \rho Z_{lo}(\mathbf{x}) + Z_d(\mathbf{x}) \tag{7}$$

The covariance matrix is constructed as

$$\mathbf{C} = \begin{pmatrix} \sigma_{lo}^2 \mathbf{\Psi}_{lo}(\mathbf{X}_{lo}, \mathbf{X}_{lo}) & \rho \sigma_{lo}^2 \mathbf{\Psi}_{lo}(\mathbf{X}_{lo}, \mathbf{X}_{hi}) \\ \rho \sigma_{lo}^2 \mathbf{\Psi}_{lo}(\mathbf{X}_h, \mathbf{X}_{lo}) & \rho \sigma_{lo}^2 \mathbf{\Psi}_{lo}(\mathbf{X}_{hi}, \mathbf{X}_{hi}) + \sigma_d^2 \mathbf{\Psi}_d(\mathbf{X}_{hi}, \mathbf{X}_{hi}) \end{pmatrix} \tag{8}$$

where $\mathbf{\Psi}_{lo}(\mathbf{X}_{lo}, \mathbf{X}_{hi})$ denotes a matrix of correlations of the form ψ_{lo} between data $\mathbf{X}_{lo}$ and $\mathbf{X}_{hi}$. Similarly, $\mathbf{\Psi}_{lo}(\mathbf{X}_{lo}, \mathbf{X}_{lo})$ denotes a matrix of correlations of the form ψ_{lo} between data $\mathbf{X}_{lo}$ and $\mathbf{\Psi}_{hi}(\mathbf{X}_{hi}, \mathbf{X}_{hi})$ denotes a matrix of correlations of the form ψ_{lo} between data $\mathbf{X}_{hi}$. Furthermore, $\mathbf{\Psi}_d(\mathbf{X}_{hi}, \mathbf{X}_{hi})$ denotes a matrix of correlations of the form ψ_d between data $\mathbf{X}_{hi}$. Here, the squared exponential kernel was selected to describe the correlation between random variables, where p_j was fixed at $p_{(1,2,...,k)} = 2$. The specific expression is as follows:

$$cor\big[Y(\mathbf{x}^{(i)}), Y(\mathbf{x}^{(l)})\big] = \exp\left(-\sum_{j=1}^{k} \theta_j \big| x_j^{(i)} - x_j^{(l)} \big|^{p_j} \right) \tag{9}$$

where k is the number of design variables, θ_j represents the correlation coefficient of j-th design variable, and $x_j^{(i)}$ is the j-th design variable of i-th sample.

The basis of cokriging is that our prediction of a new expensive sample is assumed to be consistent with the observed data and the maximum-likelihood-estimations for the model parametres. Therefore, we augmented the observed data with a predicted value and maximised the likelihood of this augmented data by varying our prediction while keeping the model parametres fixed. The augmented dataset is defined as follows:

$$\tilde{\mathbf{X}} = \begin{pmatrix} \mathbf{X}_{lo} \\ \mathbf{X}_{hi} \\ \mathbf{X} \end{pmatrix} = \left(\mathbf{x}_{lo}^{(1)} \cdots \mathbf{x}_{lo}^{(n_{lo})} \mathbf{x}_{hi}^{(1)} \cdots \mathbf{x}_{hi}^{(n_{hi})} \mathbf{x} \right)^{\mathrm{T}} \tag{10}$$

In addition, the values at locations with a predicted value are defined as

$$\tilde{\mathbf{y}} = \left(\mathbf{y}_{lo}^{\mathrm{T}} \mathbf{y}_{hi}^{\mathrm{T}} \hat{\mathbf{y}}_{hi(\mathbf{x})} \right)^{\mathrm{T}} \tag{11}$$

The new covariance matrix $\widetilde{C}$ can be expressed as

$$\tilde{C} = \begin{pmatrix} \hat{\sigma}_{lo}^2 \mathbf{\Psi}_{lo}(\mathbf{X}_{lo}, \mathbf{X}_{lo}) & \rho \hat{\sigma}_{lo}^2 \mathbf{\Psi}_{lo}(\mathbf{X}_{lo}, \mathbf{X}_{hi}) & \rho \hat{\sigma}_{lo}^2 \mathbf{\Psi}_{lo}(\mathbf{X}_{lo}, \mathbf{x}) \\ \rho \hat{\sigma}_{lo}^2 \mathbf{\Psi}_{lo}(\mathbf{X}_{hh}, \mathbf{X}_{lo}) & \rho_{lo}^2 \hat{\sigma}_{lo}^2 \mathbf{\Psi}_{lo}(\mathbf{X}_{hi}, \mathbf{X}_{hi}) + \hat{\sigma}_d^2 \mathbf{\Psi}_d(\mathbf{X}_{hi}, \mathbf{X}_{hi}) & \left(\rho^2 \hat{\sigma}_{lo}^2 + \hat{\sigma}_d^2 \right) \mathbf{\Psi}_d(\mathbf{X}_{hi}, \mathbf{x}) \\ \rho \hat{\sigma}_{lo}^2 \mathbf{\Psi}_{lo}(\mathbf{X}_{lo}, \mathbf{x})^{\mathrm{T}} & \left(\rho^2 \hat{\sigma}_{lo}^2 + \hat{\sigma}_d^2 \right) \mathbf{\Psi}_d(\mathbf{X}_{hi}, \mathbf{x})^{\mathrm{T}} & \rho^2 \hat{\sigma}_{lo}^2 + \hat{\sigma}_d^2 \end{pmatrix} \tag{12}$$

Based on the Gaussian process theory, we obtain

$$\hat{y}_{hi}(\mathbf{x}) = \hat{\mu} + \mathbf{c}^{\mathrm{T}} \mathbf{c}^{-1} \big(\mathbf{y} - \mathbf{1}\hat{\mu} \big) \tag{13}$$

where

$$\mathbf{c} = \begin{pmatrix} \rho \hat{\sigma}_{lo}^2 \mathbf{\Psi}_{lo}(\mathbf{X}_{lo}, \mathbf{x}) \\ \left(\rho^2 \hat{\sigma}_{lo}^2 + \hat{\sigma}_d^2 \right) \mathbf{\Psi}_d(\mathbf{X}_{hi}, \mathbf{x}) \end{pmatrix} \tag{14}$$

$$\hat{\mu} = \frac{\mathbf{1}^{\mathrm{T}} \mathbf{C}^{-1} \mathbf{y}}{\mathbf{1}^{\mathrm{T}} \mathbf{C}^{-1} \mathbf{1}} \tag{15}$$

Here $\mathbf{1}$ is an $n \times 1$ column vectors of ones. To obtain μ_{lo}, $\hat{\sigma}_{\text{lo}}^2$, and θ_{lo} for the low-fidelity Gaussian process $Z_{\text{lo}}(\mathbf{x})$, we can maximise the ln-likelihood as

$$-\frac{n}{2}\ln\left(\sigma_{\text{lo}}^2\right) - \frac{1}{2}\ln\boldsymbol{\Psi}_{\text{lo}}(\mathbf{X}_{\text{lo}}, \mathbf{X}_{\text{lo}}) - \frac{(\mathbf{y}_{\text{lo}} - \mathbf{1}\mu_{\text{lo}})^{\text{T}}\boldsymbol{\Psi}_{\text{lo}}(\mathbf{X}_{\text{lo}}, \mathbf{X}_{\text{lo}})^{-1}(\mathbf{y}_{\text{lo}} - \mathbf{1}\mu_{\text{lo}})}{2\sigma_{\text{lo}}^2} \tag{16}$$

The MLEs of

$$\hat{\mu}_{\text{lo}} = \frac{\mathbf{1}^{\text{T}}\boldsymbol{\Psi}_{\text{lo}}(\mathbf{X}_{\text{lo}}, \mathbf{X}_{\text{lo}})^{-1}\mathbf{y}_{\text{lo}}}{\mathbf{1}^{\text{T}}\boldsymbol{\Psi}_{\text{lo}}(\mathbf{X}_{\text{lo}}, \mathbf{X}_{\text{lo}})^{-1}\mathbf{1}} \tag{17}$$

$$\hat{\sigma}_{\text{lo}}^2 = \frac{(\mathbf{y}_{\text{lo}} - \mathbf{1}\widehat{\mu}_{\text{lo}})^{\text{T}}\boldsymbol{\Psi}_{\text{lo}}(\mathbf{X}_{\text{lo}}, \mathbf{X}_{\text{lo}})^{-1}(\mathbf{y}_{\text{lo}} - \mathbf{1}\widehat{\mu}_{\text{lo}})}{n_{\text{lo}}} \tag{18}$$

and $\widehat{\theta}_{\text{lo}}$ could be obtained by maximising the following equation after substituting Equations (17) and (18) in Equation (16):

$$-\frac{n_{\text{lo}}}{2}\ln\left(\hat{\sigma}_{\text{lo}}^2\right) - \frac{1}{2}\ln|\boldsymbol{\Psi}_{\text{lo}}(\mathbf{X}_{\text{lo}}, \mathbf{X}_{\text{lo}})| \tag{19}$$

To estimate $\mu_{\text{d}}, \sigma_{\text{d}}^2, \boldsymbol{\theta}_{\text{d}}$, and ρ, we defined the following:

$$\mathbf{d} = \mathbf{y}_{\text{hi}} - \rho\mathbf{y}_{\text{lo}}(\mathbf{X}_{\text{hi}}) \tag{20}$$

Similarly, μ_{d} and σ_{d}^2 were obtained by maximising the ln-likelihood of the expensive sample as

$$-\frac{n}{2}\ln\left(\sigma_{\text{d}}^2\right) - \frac{1}{2}\ln\boldsymbol{\Psi}_{\text{lo}}(\mathbf{X}_{\text{lo}}, \mathbf{X}_{\text{lo}}) - \frac{(\mathbf{d} - \mathbf{1}\mu_{\text{d}})^{\text{T}}\boldsymbol{\Psi}_{\text{d}}(\mathbf{X}_{\text{hi}}, \mathbf{X}_{\text{hi}})^{-1}(\mathbf{d} - \mathbf{1}\mu_{\text{d}})}{2\sigma_{\text{d}}^2} \tag{21}$$

Equation (21) yields the MLEs of the following as:

$$\hat{\mu}_{\text{d}} = \frac{\mathbf{1}^{\text{T}}\boldsymbol{\Psi}_{\text{d}}(\mathbf{X}_{\text{hi}}, \mathbf{X}_{\text{hi}})^{-1}\mathbf{d}}{\mathbf{1}^{\text{T}}\boldsymbol{\Psi}_{\text{d}}(\mathbf{X}_{\text{hi}}, \mathbf{X}_{\text{hi}})^{-1}\mathbf{1}} \tag{22}$$

$$\hat{\sigma}_{\text{d}}^2 = \frac{(\mathbf{d} - \mathbf{1}\widehat{\mu}_{\text{d}})^{\text{T}}\boldsymbol{\Psi}_{\text{d}}(\mathbf{X}_{\text{hi}}, \mathbf{X}_{\text{hi}})^{-1}(\mathbf{d} - \mathbf{1}\widehat{\mu}_{\text{d}})}{n_{\text{hi}}} \tag{23}$$

Furthermore, $\widehat{\theta}_{\text{d}}$ could be obtained by maximising the following equation after substituting Equations (22) and (23) in Equation (21)

$$-\frac{n_{\text{hi}}}{2}\ln\left(\hat{\sigma}_{\text{d}}^2\right) - \frac{1}{2}\ln|\boldsymbol{\Psi}_{\text{lo}}(\mathbf{X}_{\text{lo}}, \mathbf{X}_{\text{lo}})| \tag{24}$$

With the above derivation, it is possible to use cokriging to make effective predictions. For more details about derivation and implementation, resources could be found in Refs [41, 42].

2.4 Infill strategy

To improve the prediction accuracy of the surrogate models, the low- and high-fidelity samples must be updated after each iteration until the termination condition is achieved. Infilling low- and high-fidelity samples were generated from the current Pareto front to refine the surrogate models. Specifically, to update the high-fidelity samples, the current X_{Parete} was first clustered using the K-means clustering method. The Pareto fitness function (MG) was then calculated for each point in X_{Parete} [27, 43]:

$$G_i = 1 - \max_{j \neq i}\left[\min\left(f_{s1}^i - f_{s1}^j, \ldots, f_{sk}^i - f_{sk}^j\right)\right], i = 1, 2, \cdots, m \tag{25}$$

where G_i denotes the Pareto fitness at the i-th sampling point, and f_{sk}^i is the normalised k-th objective function at the i-th sampling point, given by

$$f_{sk}^i = \frac{f_{k,i} - f_{k,\min}}{f_{k,\max} - f_{k,\min}} \tag{26}$$

where $f_{k,i}$ is the k-th objective function at the i-th sampling point, and $f_{k,\max}$ and $f_{k,\min}$ denote the maximum and minimum values of the k-th objective function among all sampling points, respectively. When the Pareto fitness G_i is greater than one, the sampling point is a Pareto-optimal solution. A modified Pareto fitness function was calculated to construct a function that generates local minima around a set of Pareto-optimal solutions.

$$MG_i = \begin{cases} (1 - G_i) + 2 \times G_{\max} & G_i < 1 \\ G_i & G_i \geq 1 \end{cases} \quad i = 1, 2, \cdots, m \tag{27}$$

A lower MG value indicates that the sample is closer to the Pareto front, and the sample point with the minimum MG value in each cluster was selected as the high-fidelity infill sample point, as follows:

$$x_{\text{infill}}^{(k)} = \arg \min MG(x) \text{ with } x \in X_k, k = 1, 2, \cdots, k_c \tag{28}$$

where X_k is the sample set of the k-th cluster and $\chi_{\text{infill}}^{(k)}$ are the selected high-fidelity infill samples. Specifically, all Pareto fronts were selected to update the low-fidelity samples.

With the high-fidelity and low-fidelity infill strategies described above, both exploration and exploitation could be performed.

2.5 Genetic algorithm

The NSGA-II, originally proposed by Deb, was adopted in this study because of its proven capabilities for global optimisation in flow aerodynamic applications. NSGA-II generates offspring using specific types of crossover and mutation and then selects the next generation according to a non-dominated sorting and crowding distance comparison. The initial seed was set at 36, with 36 individuals in the following generation and a total of 5,000 generations. The mutation probability was set at 0.1 and the crossover rate was set at 0.9. The selection operator was set as a tournament, the mutation operator was set as a polynomial mutation, and the crossover operator was set as the simulated binary crossover.

2.6 Validation and verification

Two test functions were used to validate the effectiveness of the MO-ACK framework. To demonstrate the role of multi-fidelity, a multi-objective optimisation framework based on kriging (MO-AK) was also tested. Comprehensive evaluation indicators were introduced to evaluate the performance of the multi-objective optimisation process, such as the hypervolume (HV) indicator [44] and inverted generational distance (IGD) indicator [45]. In this study, the HV indicator was calculated through optimisation iterations to measure the convergence and diversity of the Pareto front solutions. A higher value of HV indicates better capability for exploring the Pareto front. As shown in Fig. 11, the two main factors in the HV indicator are the reference point and the non-dominated solution. When non-dominated solutions are obtained, a reference point must be validated. A schematic of a 2D HV indicator is shown in Fig. 11. The HV indicator used in higher dimensional problems follows this analogy.

2.6.1 FON test function optimisation

The definition of the FON two-objective test function, composed of high-fidelity and low-fidelity functions, is as follows [46]:
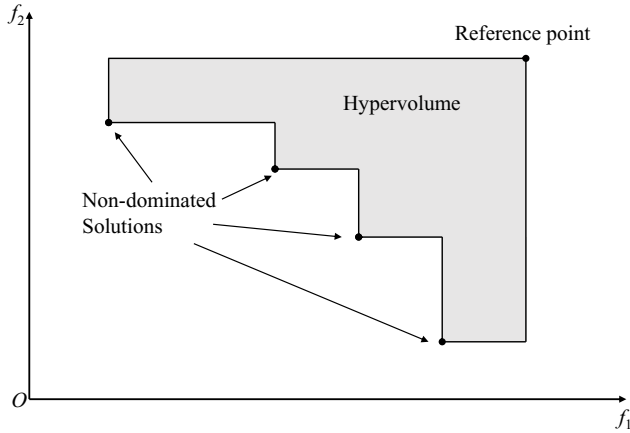
Figure 11. *Schematic of a 2D HV indicator.*

$$\text{Minimise: } f_1(x_1, x_2, \cdots, x_5) = 1 - \exp\left(-\sum_{i=1}^{5}\left(x_i - \frac{1}{\sqrt{5}}\right)^2\right)$$

$$\text{Minimise: } f_2(x_1, x_2, \cdots, x_5) = 1 - \exp\left(-\sum_{i=1}^{5}\left(x_i + \frac{1}{\sqrt{5}}\right)^2\right)$$

$$\text{Minimise: } f_{11}(x_1, x_2, \cdots, x_5) = 1 - \exp\left(-\sum_{i=1}^{5}\left(0.5x_i - 0.1 - \frac{1}{\sqrt{5}}\right)^2\right)$$

$$\text{Minimise: } f_{12}(x_1, x_2, \cdots, x_5) = 1 - \exp\left(-\sum_{i=1}^{5}\left(0.6x_i + 0.1 + \frac{1}{\sqrt{5}}\right)^2\right)$$

$$(29)$$

where f_1 and f_2 denote the high-fidelity functions, and f_{11} and f_{12} denote the low-fidelity functions. The design space of the test function is $x_1, x_2, \cdots, x_5 \in [-4, 4]$.

The optimisation routine was initialised with LHS to create 20 initial high-fidelity samples and 40 initial low-fidelity samples. During each iteration, the high-fidelity samples were updated by adding five samples using the high-fidelity infill strategy. Meanwhile, the low-fidelity samples were updated by adding 10 samples, including the samples added to the high-fidelity samples using the low-fidelity infill strategy. The optimisation routine ended when the prescribed 24 iterations were met. This was consecutively tested in eight trials. The results of the eight trials are shown in Fig. 12. Moreover, 500,000 samples were generated by LHS, and the HV was calculated as the reference, as shown in Fig. 12.

As observed from Fig. 12, the MO-ACK model outperformed the MO-AK model in terms of achieving higher diversity because its HV was larger after five iterations in all trials. Eight trials were initialised with random LHS; therefore, the initial HV values were different. Both MO-ACK and MO-AK performed better than the reference. It can also be observed from the boxplots of the HV values from the eight trials that the MO-ACK has a larger mean HV value than the MO-AK. The NSGA-II was also included for comparison. The population size was set to 28 and the maximum generation was set to 20. As shown in Fig. 13, the NSGA-II exhibited the worst performance.

In comparison to the MO-AK model, we can conclude that the MO-ACK model can effectively explore the Pareto front of a relatively low-dimension optimisation problem.

2.6.2 DTLZ2 test function optimisation
The definition of the DTLZ2 three-objective test functions, composed of high-fidelity and low-fidelity functions, is as follows [46]:
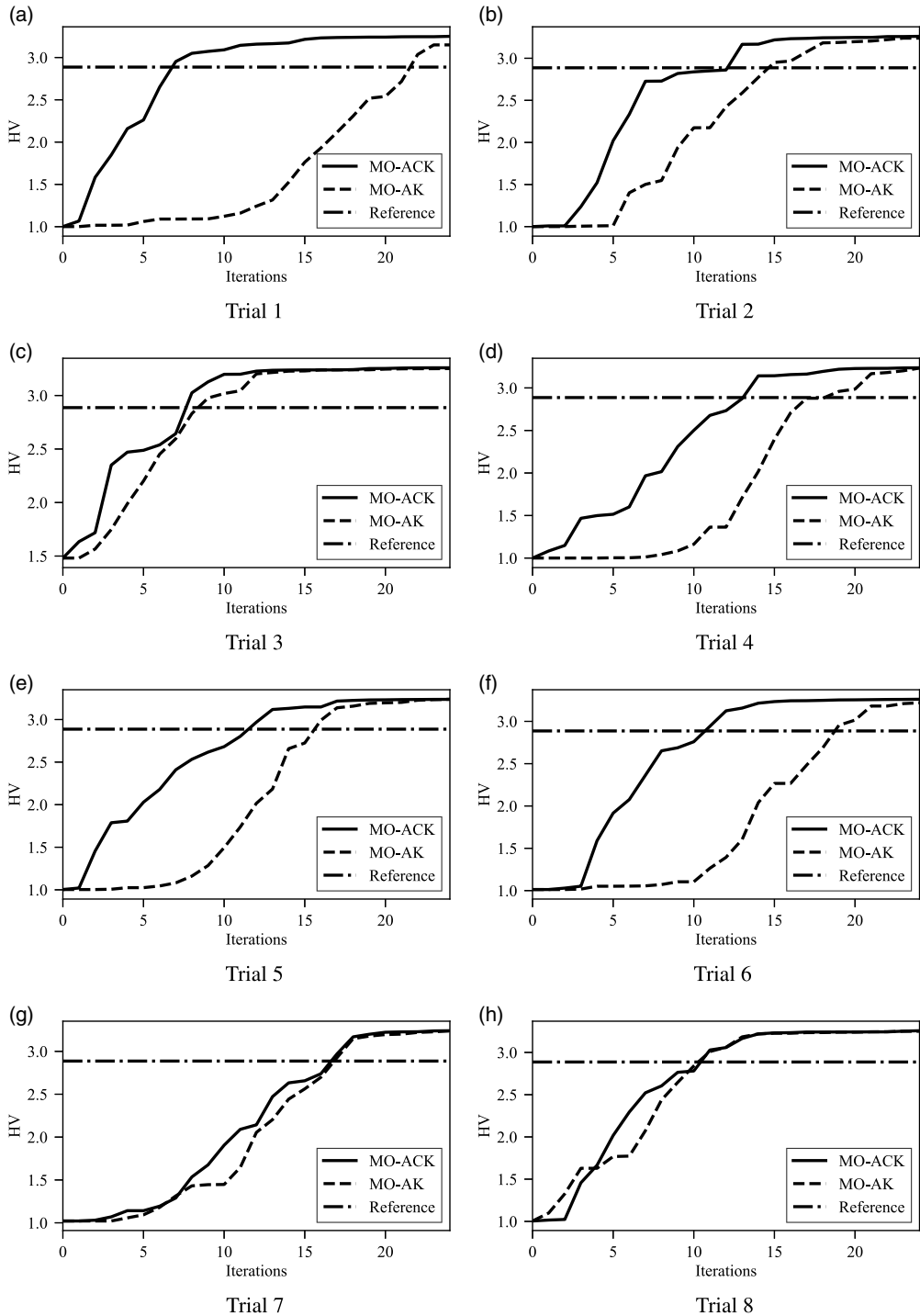
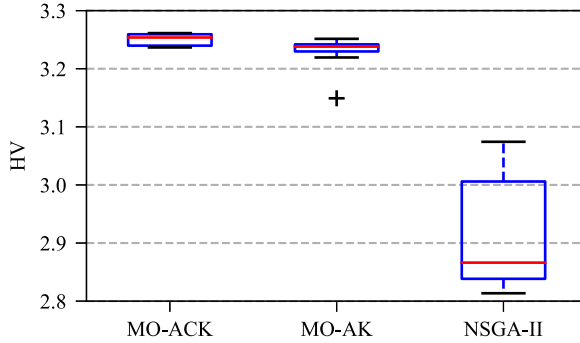*Figure 12. HV results of the FON test function.*

Figure 13. *Boxplots of the HV values of the FON test function from the eight trials.*

$$\text{Minimise: } f_1(x_1, x_2, \cdots, x_{18}) = (1 + g) \cos(0.5x_1\pi) \cos(0.5x_2\pi)$$

$$\text{Minimise: } f_2(x_1, x_2, \cdots, x_{18}) = (1 + g) \cos(0.5x_1\pi) \sin(0.5x_2\pi)$$

$$\text{Minimise: } f_3(x_1, x_2, \cdots, x_{18}) = (1 + g) \sin(0.5x_1\pi)$$

$$g = \sum_{i=3}^{18} (x_i - 0.5)^2$$

$$f_{11}(x_1, x_2, \cdots, x_{18}) = (0.5 + 1.5g) \cos(0.6x_1\pi) \cos(0.4x_2\pi),$$

$$f_{12}(x_1, x_2, \cdots, x_{18}) = (0.3 + 1.2g) \cos(0.4x_1\pi) \sin(0.6x_2\pi),$$

$$f_{13}(x_1, x_2, \cdots, x_{18}) = (0.4 + 1.3g) \sin(0.5x_1\pi)$$

$$g_c = \sum_{i=3}^{18} (0.8x_i - 0.3)^2$$

(30)

where f_1, f_2, and f_3 denote the high-fidelity functions, and f_{11}, f_{12}, and f_{13} denote the low-fidelity functions. Furthermore, the design space of the test function is $x_1, x_2, \cdots, x_{18} \in [0, 1]$.

The optimisation routine was initialised with LHS to create 120 initial high-fidelity samples and 240 initial low-fidelity samples. During each iteration, the high-fidelity samples were updated by adding 18 samples using the high-fidelity infill strategy. Meanwhile, the low-fidelity samples were updated by adding 36 samples, including the samples added to the high-fidelity samples using the low-fidelity infill strategy. The optimisation routine ended when the four prescribed iterations were met. This was consecutively tested in eight trials. The results of the eight trials are shown in Fig. 14. Moreover, 500,000 samples were generated by LHS, and the HV was calculated as the reference, as shown in Fig. 14.

As observed from Fig. 14, the MO-ACK model outperformed the MO-AK model in terms of achieving higher diversity because its HV was larger after five iterations in all trials. Eight trials were initialised with random LHS; therefore, the initial HV values were different. All eight trials of the MO-ACK obtained higher HV values than the reference, whereas all eight trials of the MO-AK obtained lower HV values. It can also be observed from the boxplots of the HV values from the eight trials that the MO-ACK has a larger mean HV value than the MO-AK. The NSGA-II was also included for comparison. The population size was set to 32, and the maximum generation was set to 6. As shown in Fig. 15, the NSGA-II exhibited the worst performance.

We may infer that the MO-ACK model can more effectively explore the Pareto front of a high-dimensional optimisation problem than the MO-AK model.
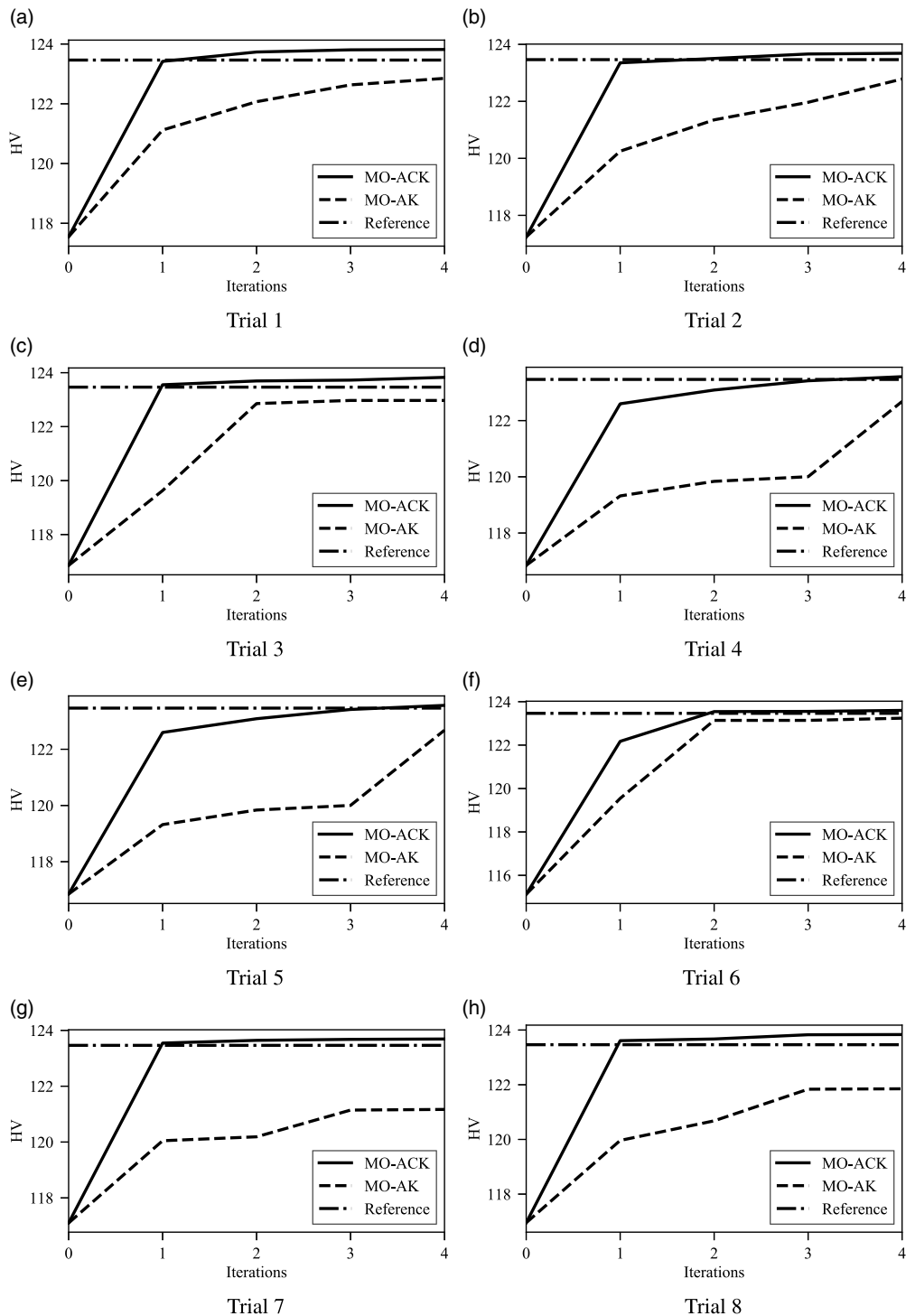
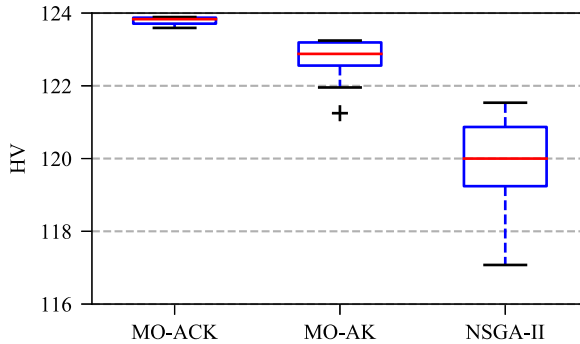**Figure 14.** *HV results of the DTLZ2 test function.*

Figure 15. *Boxplots of the HV values of the DTLZ2 test function from the eight trials.*

3.0 Results and discussion

The proposed optimisation framework was adopted to investigate the aerodynamic shape optimisation of an aero-engine nacelle under different operating conditions. The optimisation routine was initialised with LHS to create 120 initial high-fidelity samples and 240 initial low-fidelity samples. Subsequently, the iCST method was applied to construct the nacelle geometry, which was input to ANSYS ICEM to automatically create a structured mesh using a custom script. Computations were carried out using an in-house solver to obtain the target values. The obtained data were then processed and passed to a surrogate model as input. The Pareto front was explored using the NSGA-II. During each iteration, the high-fidelity samples were updated by adding four samples using the high-fidelity infill strategy. Meanwhile, the low-fidelity samples were updated by adding eight samples, including the samples added to the high-fidelity samples, using the low-fidelity infill strategy. The optimisation routine ended when the prescribed maximum iterations were met. To compare the ability to explore the Pareto front of different optimisation strategies, the MO-AK-based optimisation was also applied. To eliminate the influence of the initial samples, same high-fidelity initial samples were used for both MO-ACK-based optimisation and MO-AK-based optimisation.

Three aero-lines were used to construct the geometry of the non-axisymmetric nacelle. Each aero-line was controlled using six design variables (r_{if}, r_{max}, f_{max}, β_{nac}, r_i, and f_i). The lower and upper bounds of these six parametres were the same for each aero-line, as listed in Table 5.

Two nacelle performance metrics were employed as the objective functions for the optimistion routine. The drag coefficient ($C_{D-cruise}$) was evaluated under cruise conditions, whereas the intake pressure recovery (IPR) was evaluated under takeoff conditions. To assess the fancowl drag, the method described by Christie et al. [47] was used, which uses surface integrals, velocity, and pressure distribution on the AIP and the farfield state to compute the sum of the forces on the entry streamtube and fancowl, ignoring the forces on the post-exit streamtube at data flow conditions of the nozzle.

Here, $C_{D-cruise}$ was defined as the ratio of the drag force at the fancowl to the force produced by the dynamic pressure multiplied by the area at highlight, as follows:

$$C_{D-cruise} = \frac{D_{nac}}{\frac{1}{2}\rho_\infty V_\infty^2 A_{hi}} \tag{31}$$

Furthermore, $IPR_{takeoff}$ was defined as the ratio of the mean total pressure at the fanface to the total pressure of the freestream, as follows:

$$IPR_{takeoff} = \frac{\bar{P}_{0,\,fanface}}{P_0} \tag{32}$$

After the optimisation routine, the Pareto front in terms of $C_{D-cruise}$) and $IPR_{takeoff}$ is graphically shown in Fig. 16. To exhibit the Pareto front in the lower left, the Y-axis data are represented using $1 - IPR_{takeoff}$

Table 5. *Design variable bounds*

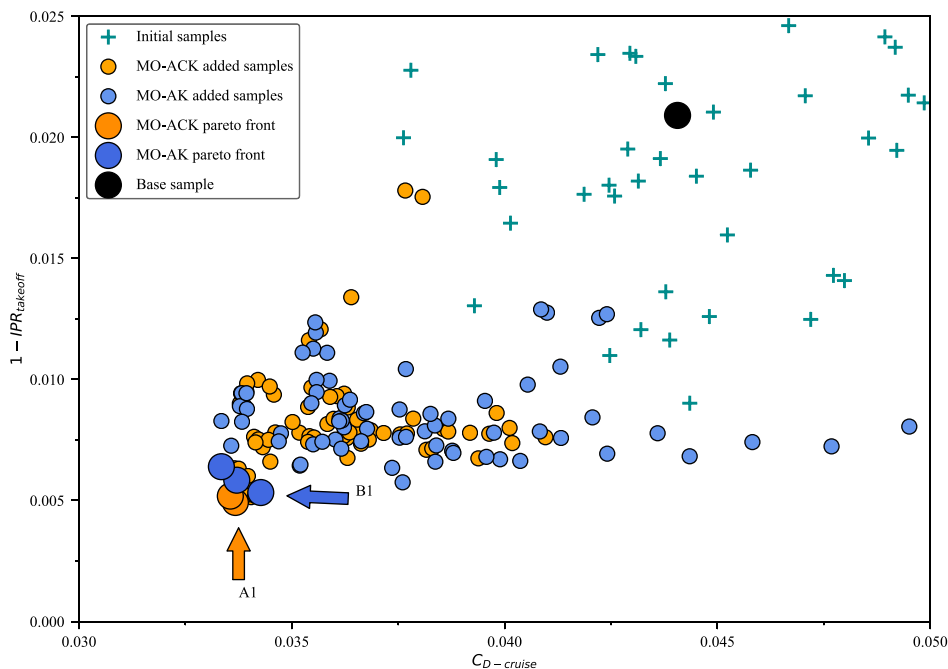| Aero-line location	Parametre	Upper bound	Lower bound
$\Phi = 0°, 90°, 180°$	r_{if}	0.08	0.04
	r_{max}	2.05	1.87
	f_{max}	0.42	0.3
	β_{nac}	15	9
	r_i	1.52	1.37
	f_i	0.42	0.28

Figure 16. *Pareto fronts for MO-AK and MO-ACK.*
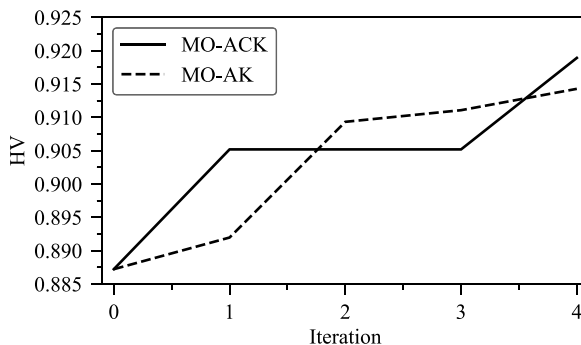
Figure 17. *Comparisons of HV between the results of MO-AK and MO-ACK.*

Table 6. *Comparison of the optimisation results from the MO-ACK and MO-AK optimisation frameworks*

Model	No. of high-fidelity samples	No. of low-fidelity samples	HV	Initial HV	Increment (%)
MO-ACK	120 + 72	240 + 144	0.9189	0.8872	3.57
MO-AK		0	0.9143		3.05

instead of IPR_{takeoff}. This Pareto front consisted of all the samples evaluated during the optimisation routine, where the added and initial samples are marked with "o" and "+", respectively. Specifically, the samples added by the MO-ACK-based method are colored orange, whereas the samples added by the MO-AK-based method are colored blue. The non-dominated solutions are highlighted with a larger marker "o". As shown in Fig. 16, the added samples are mainly clustered in the lower left, where the solutions are much closer to the Pareto front than the initial samples. The Pareto front from the MO-ACK shows a significant improvement in the convergence and diversity of solutions over the Pareto front from the MO-AK. It is also quantitatively described using the HV metrics, as shown in Fig. 17. It can be seen that the first increase in HV from the MO-ACK-based optimisation framework is 0.0180, whereas it is only 0.0047 from the MO-AK-based optimisation framework. Moreover, the HV from the MO-ACK-based optimisation framework ends with a value of 0.9189 after the 4th iteration, whereas the MO-AK-based optimisation framework ends with a value of 0.9143. It is clear that the MO-ACK-based optimisation framework can achieve a higher HV value, which means finding better solutions in terms of convergence and diversity, compared to the MO-AK-based optimisation framework. It can be found that with the help of the low-fidelity samples, the MO-ACK-based optimisation framework can more efficiently explore the design space. These results are summarised in Table 6.

The results of the optimisation routine under different conditions are discussed below. Because the Pareto solutions are mutually non-dominated, they are all feasible and acceptable in engineering practices. To better illustrate the effectiveness of the optimisation framework, a more detailed investigation of the nacelle designs with the highest IPR_{takeoff} identified using the MO-ACK and MO-AK models, referred to as A1 and B1, respectively, was carried out. The base sample was axisymmetric; therefore, the scarf angle was zero.

The comparison of the baseline and the optimal nacelle geometry designs of A1 and B1 is shown in Fig. 18. In comparison to the azimuthal section $\psi = 0°$, $\psi = 90°$ and $\psi = 180°$ of the baseline, the three lines of both optimal nacelle geometry designs of A1 and B1 are thinner. For the azimuthal section $\psi = 0°$, design B1 has highest rates of change in curvature, corresponding to the highest peaks in isentropic Mach number. For the azimuthal section $\psi = 90°$, design A1 has highest rates of change in curvature. For the azimuthal section $\psi = 180°$, the rates of change in curvature of design B1 is slightly larger than that of design A1. In all azimuthal sections, design A1 and design B1 have smaller boat-tail angles than base sample. For the intake geometry, design A1 and design B1 are similar in all azimuthal sections and have a smaller thickness compared to the base sample. The following is a further flow field analysis.

3.1 Results under cruise condition

Designs A1 and B1 exhibited significant reductions in terms of $C_{D-\text{cruise}}$ compared to the configuration of the base sample. While design A1 exhibited a reduction of 23.6% while design B1 exhibited a reduction of 22.2%. As shown in Fig. 19, the large variation in the nacelle drag characteristics was caused by a fundamental change in the associated nacelle transonic flow aerodynamics. The pressure distributions of all designs are shown in Fig. 20. As shown in Fig. 21, the isentropic Mach number distributions of the base sample configuration on all four aero-lines were almost the same because of their axisymmetric characteristics. The location of the peak isentropic Mach number at the top aero-line ($\psi = 0°$) was significantly different for the three selected designs and varied by 2.474. Design A1, which had the
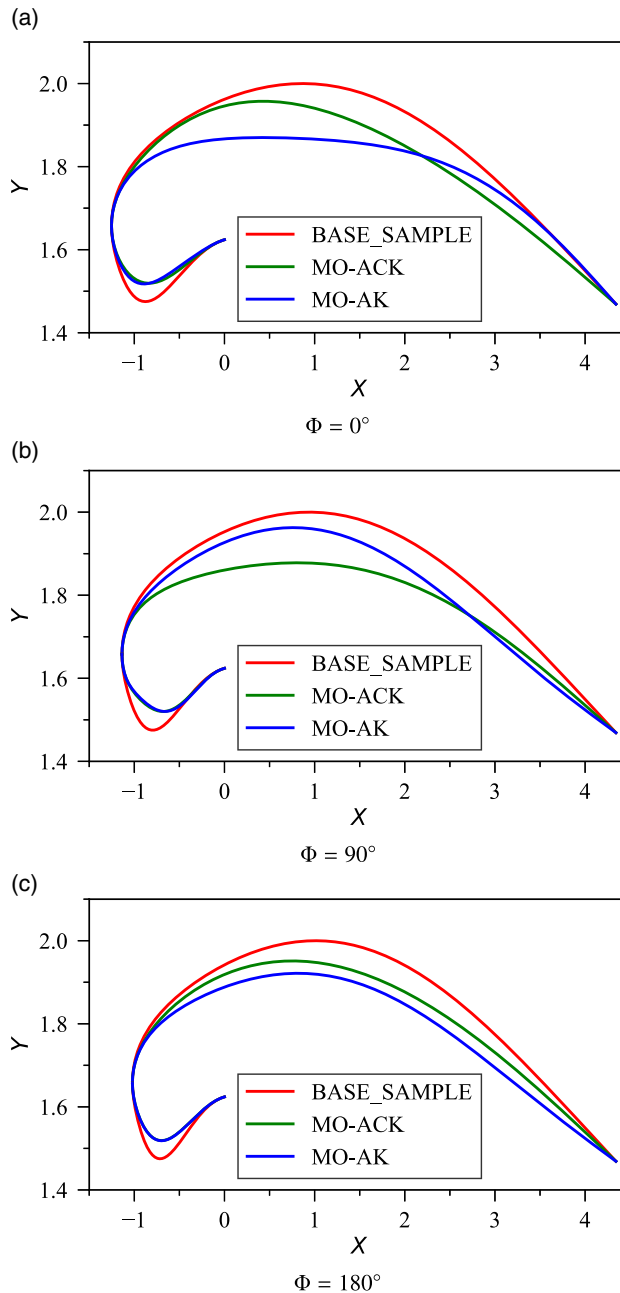
(a)

$\Phi = 0°$

(b)

$\Phi = 90°$

(c)

$\Phi = 180°$

Figure 18. *Comparisons of the nacelle geometry for the selected designs at different azimuthal sections.*

highest IPR_{takeoff} found throughout the optimisation process, had an initial acceleration to terminate with a strong shockwave at $X = 0.14$. Design A1 had a well-defined shockwave at $X = 0.14$, whereas the configuration of the base sample had a similar shockwave at $X = 1.697$. Compared to the other two configurations, design B1 had a shockwave in the shortest position at $X = -0.777$. Unlike the other two, which experienced accelerations at the start, design B1 experienced a stable process at the beginning. For the azimuthal section $\psi = 45°$, design A1 had a similar benign transonic flow structure compared to
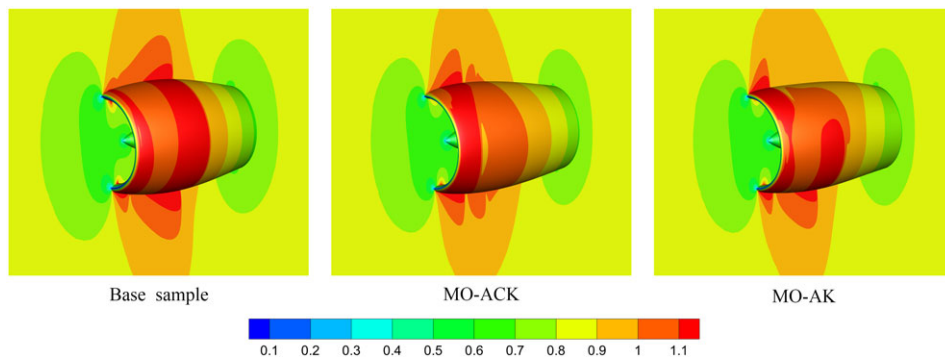
Figure 19. *Comparison of the isentropic Mach number contours for the selected designs.*
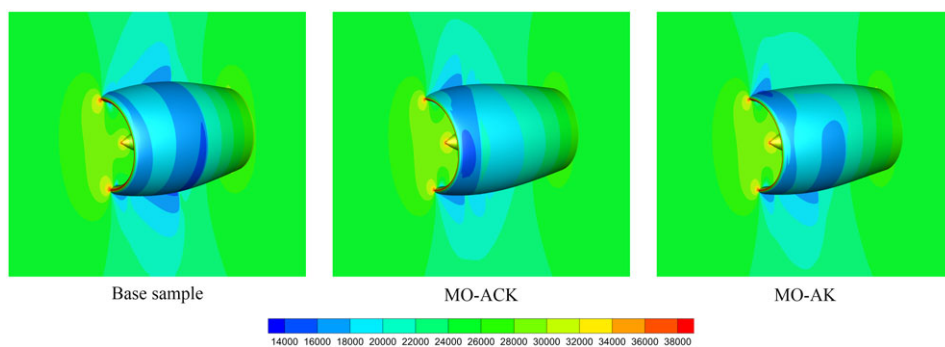
Figure 20. *Comparison of the pressure contours for the selected designs.*

design B1. For the azimuthal section $\psi = 90°$, design A1 had a well-defined shock wave at $X = -0.325$. Design B1 and the configuration of the base sample had similar flow structures except for the intensity of the associated transonic flow aerodynamics. For instance, the configuration of the base sample had an isentropic Mach number of 1.207, whereas design B1 had a Mach number of 1.177. For the azimuthal section $\psi = 180°$, design B1 still had flow structures similar to those of the base sample. Design B1 had a double shockwave structure with the first shockwave located at $X = -0.370$ and the second shockwave at $X = 1.510$. The base sample had a double shockwave structure with the first shockwave located at $X = -0.322$ and the second shockwave at $X = 1.870$. Design A1 had an initial acceleration and terminated with a shockwave at $X = 0.245$.

The design with the largest radius of curvature at the azimuthal section $\psi = 0°$ and $\psi = 90°$ has the highest peaks in isentropic Mach number, which is consistent in Figs 18 and 21. For the azimuthal section $\psi = 180°$, design A1 and design B1 have similar geometric configurations, but there is a significant difference at isentropic Mach number distributions, which indicates the sensitivity of the flow field to geometry and the strong nonlinearity of the transonic flow aerodynamics.

3.2 Results under takeoff condition

Designs A1 and B1 had significant improvements in terms of IPR_{takeoff} compared to the configuration of the base sample. While design A1 had a reduction of 1.63%, design B1 had 1.59%. In Fig. 22, the total pressure distribution on the fanface under the takeoff condition is clearly illustrated. For the base sample, there was a distinct low-pressure area at the lower part of the fanface. This may occur because of the flow separation induced by the shockwave or adverse pressure gradient. This is an undesirable situation
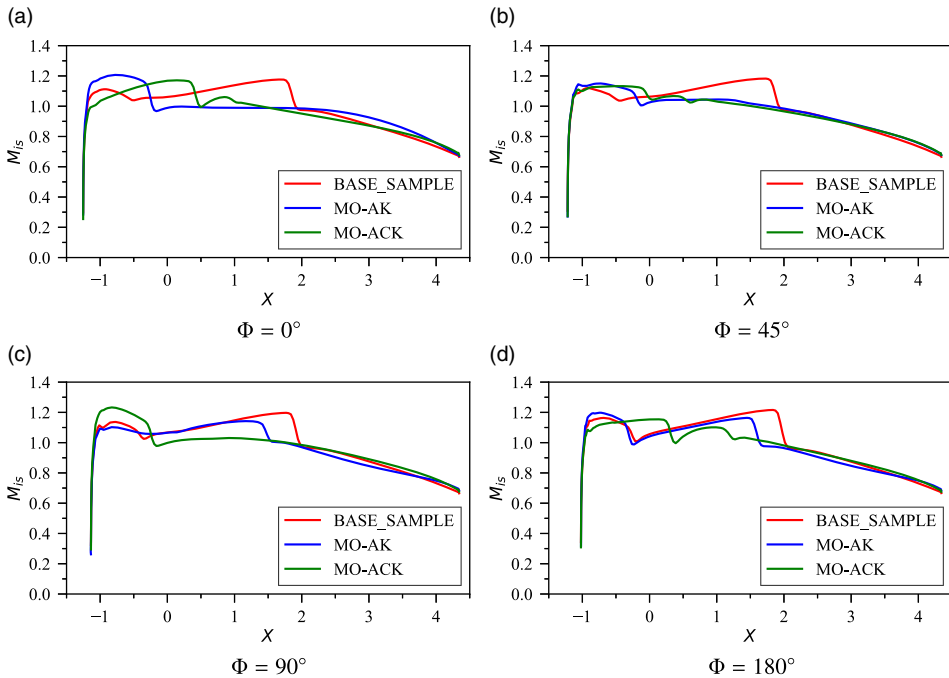
Figure 21. *Comparisons of the isentropic Mach number for the selected designs at different azimuthal sections.*
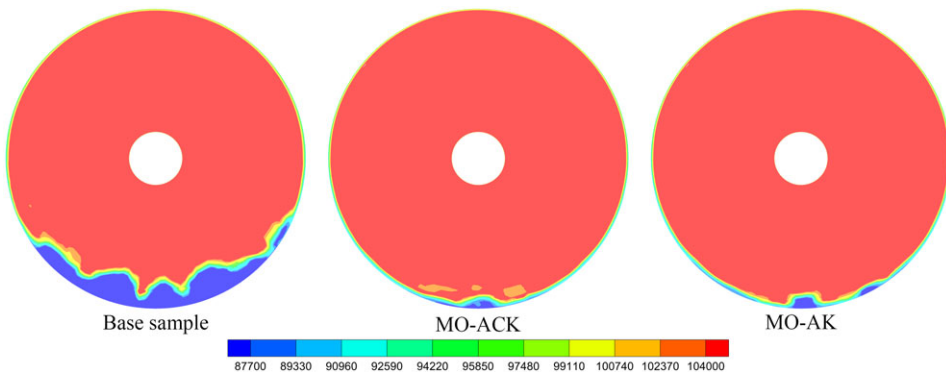

Figure 22. *Contours of the total pressure at the fanface for the selected designs.*

during takeoff. If internal separation occurs, the resulting fan entrance distortion could be critical to causing excessively high fan-blade stresses and may even cause core-compressor stalls. Designs A1 and B1 had significant improvements in $IPR_{takeoff}$ compared to the base sample. As shown in Fig. 22, the low-pressure area at the lower part of the fanface of designs A1 and B1 became significantly smaller. This also indicates that the $IPR_{takeoff}$ was higher. As shown in Fig. 18, design A1 and design B1 are similar in all azimuthal sections and have a smaller thickness compared to the base sample. Combined with the flow field analysis in Fig. 22, these designs allow for a lower total pressure loss when the airflow reaches the fan surface. Compared to design B1, the low-pressure area of design A1 was smaller and more concentrated in the lower part.
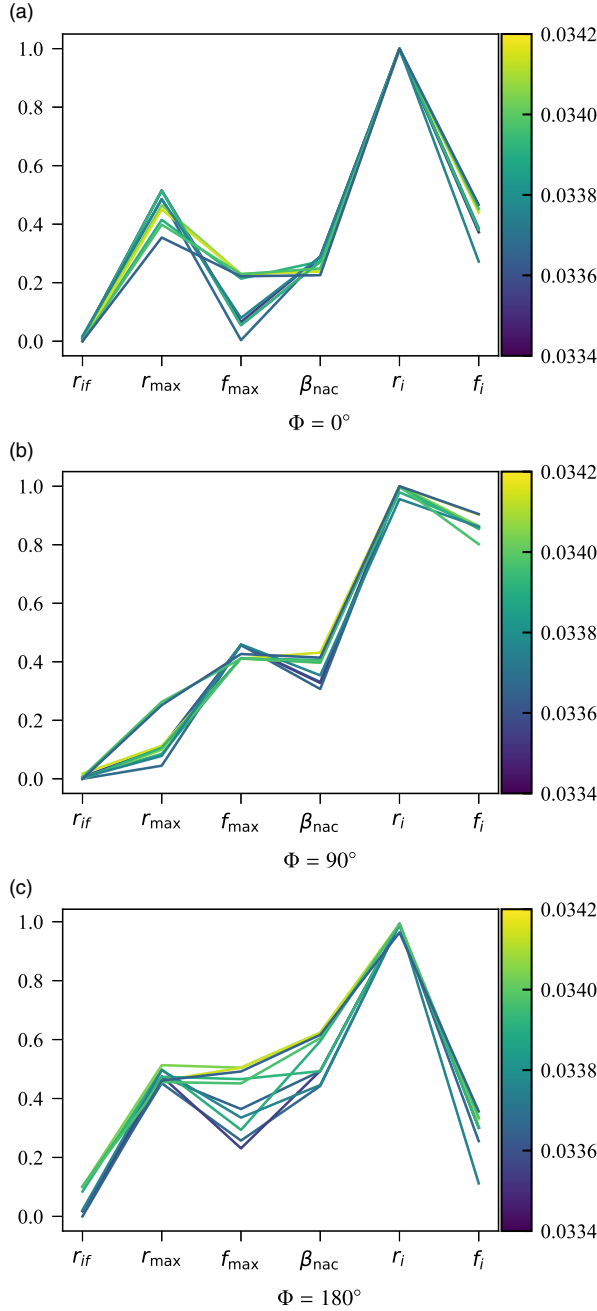
Figure 23. *Parallel coordinates plot of optimised designs coloured by $C_{D-\text{cruise}}$.*

3.3 Influence of the design variables on the nacelle performance

Parallel coordinate plots represent the regions of the design space where the non-dominated solutions are concentrated [15]. Here the ten samples of MO-ACK closest to the origin are selected as in Fig. 1, and the distance criterion formula is defined as follows:

$$distance = \sqrt{(C_{D-\text{cruise}} - 0.03)^2 + (1 - IPR_{\text{takeoff}})^2} \tag{33}$$
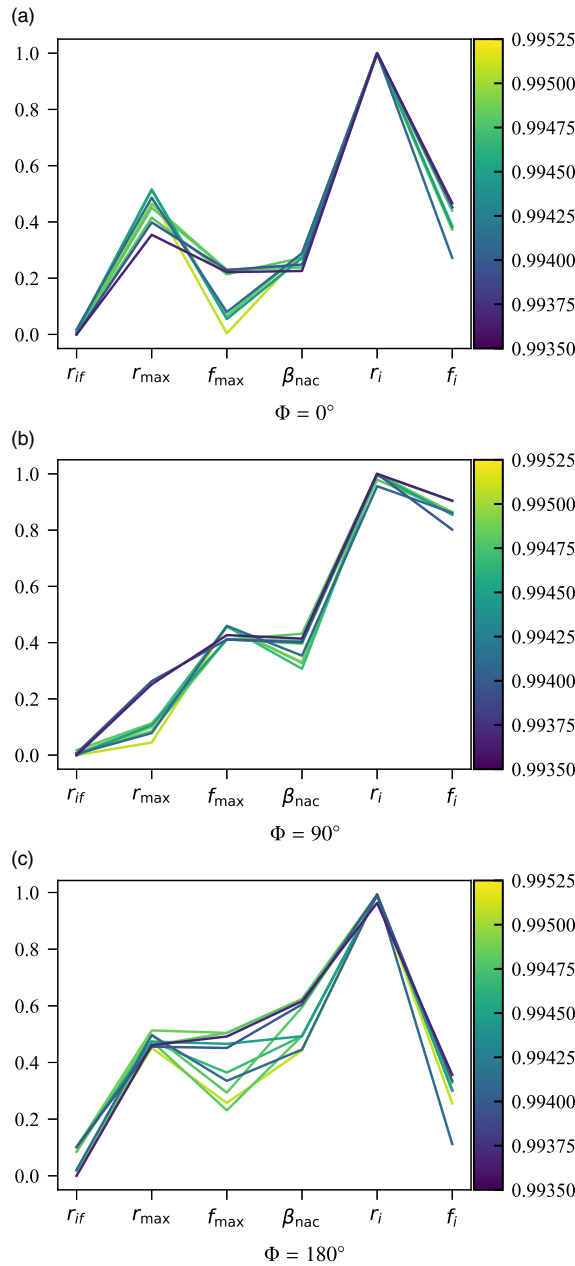
Figure 24. *Parallel coordinates plot of optimised designs coloured by IPR$_{\text{takeoff}}$.*

Parallel coordinates plot of optimised designs coloured by $C_{D-\text{cruise}}$ is shown in Fig. 23. Parallel coordinates plot of optimised designs coloured by IPR_{takeoff} is shown in Fig. 24. The figures show that the range of variation of design variables r_{if} and r_i is small in all azimuthal sections and converges to the design space boundary. This provides some guidelines for design space considerations for subsequent preliminary designs. The overall trend of the design parametres is consistent in the azimuthal section $\psi = 0°$ and azimuthal section $\psi = 180°$, and differs significantly from azimuthal section $\psi = 90°$. In the azimuthal section $\psi = 0°$, design variable f_{max} has the largest range of variation, which is consistent in the azimuthal section $\psi = 180°$, but in the azimuthal section $\psi = 90°$, design variable r_{max} has the

largest range of variation. Overall, the range of design variables changed the least in the azimuthal section $\psi = 90°$ and the most in the azimuthal section $\psi = 180°$. This is likely because throughout the multi-objective optimisation process, the takeoff condition was taken into account but the crosswind condition was not. This also demonstrates the complexity of multi-objective optimisation of non-axisymmetric nacelles.

4.0 Conclusion

In this study, a novel multi-fidelity surrogate-based multi-objective optimisation framework was proposed. The framework was compared to a conventional single-fidelity surrogate-based multi-objective optimisation framework to verify the effect of multi-fidelity. The two-objective and three-objective test functions were adopted, and the results show that with the help of a low-fidelity dataset, the optimisation method can find the Pareto solutions with better convergence and higher diversity.

The proposed MO-ACK framework was also applied to the aerodynamic shape optimisation of a non-axisymmetric nacelle. It encompassed several fundamental modules, including LHS, geometry parameterisation based on iCST, automatic mesh generation using ANSYS ICEM, CFD numerical analysis using an in-house solver, cokriging-based model, NSGA-II, and an infilling method for both high-fidelity and low-fidelity data. The two-objective and three-objective test functions were used to validate the effectiveness of the proposed framework. The results show that the MO-ACK outperformed the MO-AK and NSGA-II in terms of Pareto-front exploration. The optimised nacelles on the Pareto front from both optimisation strategies showed better aerodynamic performance than the base sample, which means a higher pressure-recovery ratio in the fanface under takeoff conditions and lower drag under cruise conditions. Compared to the results of the MO-AK framework optimisation, the Pareto front obtained from the MO-ACK framework optimisation had a higher HV value, which increased by 4.1% and 3.5% compared to the initial HV value. The nacelle designs with the highest IPR_takeoff of the Pareto front identified with the configuration of the MO-ACK and MO-AK frameworks were selected as the optimised designs and referred to as A1 and B1, respectively. In terms of $C_{D-\text{cruise}}$), designs A1 and B1 had significant reductions compared to the configuration of the base sample. While design A1 had a reduction of 23.6%, design B1 had a reduction of 22.2%. In terms of IPR_takeoff, designs A1 and B1 had significant improvements compared to the configuration of the base sample. While design A1 had a reduction of 1.63%, design B1 had a reduction of 1.59%. Therefore, it can be concluded that the proposed optimisation framework can be applied to the aerodynamic shape optimisation of engine nacelles under cruise and takeoff conditions.

References

[1] Raghunathan, S., Benard, E. and Watterson, J.K. Key aerodynamic technologies for aircraft engine nacelles, *Aeronaut. J.*, 2006, **110**, (1107), pp 265–288. doi: 10.1017/S0001924000013154

[2] Krein, A. and Williams, G. Flightpath 2050: Europe's vision for aeronautics, *Innovat. Sustain. Aviat. Global Environ.: Proc. Sixth Eur. Aeronaut. Days*, 2012, **30**, pp 63–71. doi: 10.3233/978-1-61499-063-5-63

[3] Birch, N.T. 2020 vision: the prospects for large civil aircraft propulsion, *Aeronaut. J.*, 2000, **104**, (1038), pp 347–352. doi: 10.1017/S0001924000063971

[4] Guha, A. Optimum fan pressure ratio for bypass engines with separate or mixed exhaust streams, *J. Propul. Power*, 2001, **17**, (5), pp 1117–1122. doi: 10.2514/2.5852

[5] Peters, A., Spakovszky, Z.S., Lord, W.K. and Rose, B. Ultrashort nacelles for low fan pressure ratio propulsors, *J. Turbomach.*, 2015, **137**, (2), 21001. doi: 10.1115/1.4028235

[6] Silva, V.T., Lundbladh, A., Petit, O. and Xisto, C. Multipoint aerodynamic design of ultrashort nacelles for ultrahigh-bypass-ratio engines, *J. Propul. Power*, 2022, **38**, (4), pp 541–558. doi: 10.2514/1.B38497

[7] Magrini, A., Buosi, D. and Benini, E. Maximisation of installed net resulting force through multi-level optimisation of an ultra-high bypass ratio engine nacelle, *Aerosp. Sci. Technol*, 2021, **119**, 107169. doi: 10.1016/j.ast.2021.107169

[8] Magrini, A., Buosi, D. and Benini, E. Analysis of installation aerodynamics and comparison of optimised configuration of an ultra-high bypass ratio turbofan nacelle, *Aerosp. Sci. Technol.*, 2022, **128**, 107756. doi: 10.1016/j.ast.2022.107756

[9] Song, W. and Keane, A.J. Surrogate-based aerodynamic shape optimization of a civil aircraft engine nacelle, *AIAA J.*, 2007, **45**, (10), pp 2565–2574. doi: 10.2514/1.30015

[10] Fang, X., Zhang, Y., Li, S. and Chen, H. Transonic nacelle aerodynamic optimization based on hybrid genetic algorithm, *In 17th AIAA/ISSMO Multidisciplinary Analysis and Optimization Conference,* 2016, p. 3833. doi: 10.2514/6.2016-3833

[11] Zhong, Y. and Li, S. A 3D shape design and optimization method for natural laminar flow nacelle, *Proc. ASME Turbo Expo*, 2017, **1**, pp 1–10. doi: 10.1115/GT2017-64379

[12] Yao, Y., Ma, D. and Yang, M. Adaptive-surrogate-based robust optimization of transonic natural laminar flow nacelle, *Chin. J. Aeronaut.*, 2021, **34**, (10), pp 36–52. doi: 10.1016/j.cja.2021.01.007

[13] Robinson, M., MacManus, D.G., Heidebrecht, A. and Grech, N. An optimization method for nacelle design, *In AIAA SciTech Forum – 55th AIAA Aerosp. Sci. Meeting*, 2017, pp 1–17. doi: 10.2514/6.2017-0708

[14] Robinson, M., MacManus, D.G., Richards, K. and Sheaf, C. Short and slim nacelle design for ultra-high BPR engines, *In AIAA SciTech Forum – 55th AIAA Aerosp. Sci. Meeting*, 2017, pp 1–13. doi: 10.2514/6.2017-0707

[15] Tejero, F., Robinson, M., MacManus, D.G. and Sheaf, C. Multi-objective optimisation of short nacelles for high bypass ratio engines, *Aerosp. Sci. Technol.*, 2019, **91**, pp 410–421. doi: 10.1016/j.ast.2019.02.014

[16] Tejero, F., MacManus, D.G. and Sheaf, C. Surrogate-based aerodynamic optimisation of compact nacelle aero-engines, *Aerosp. Sci. Technol.*, 2019, **93**, 105207. doi: 10.1016/j.ast.2019.05.059

[17] Robinson, M., MacManus, D.G. and Christie, R. Nacelle design for ultra-high bypass ratio engines with CFD based optimisation, *Aerosp. Sci. Technol.*, **113**, 106191. doi: 10.1016/j.ast.2020.106191

[18] Tejero, F., Christie, R., MacManus, D. and Sheaf, C. Non-axisymmetric aero-engine nacelle design by surrogate-based methods, *Aerosp. Sci. Technol.*, 2021, **117**, 106890. doi: 10.1016/j.ast.2021.106890

[19] Schreiner, B.D.J., Tejero, F., MacManus, D.G. and Sheaf, C. Robust aerodynamic design of nacelles for future civil aero-engines, *ASME Turbo Expo 2020: Power Land, Sea, Air*, 2020. doi: 10.1115/GT2020-14470

[20] Cipriani, F. Surrogate Modelling for Short Intake Design: University of Padua, 2017. https://thesis.unipd.it/handle/20.500.12608/25048

[21] Sanchez Moreno, F., MacManus, D. and Hueso Rebassa, J. Optimization of installed compact and robust nacelles using surrogate models, *33rd Congr. Int. Council Aeronaut. Sci.*, 2022. https://dspace.lib.cranfield.ac.uk/handle/1826/18444

[22] Kampolis, I.C. and Giannakoglou, K.C. A multilevel approach to single- and multiobjective aerodynamic optimization, *Comput. Methods Appl. Mech. Eng.*, 2008, **197**, (33-40), pp 2963–2975. doi: 10.1016/j.cma.2008.01.015

[23] Kennedy, M.C. and O'Hagan, A. Predicting the output from a complex computer code when fast approximations are available, *Biometrika*, 2000, **87**, (1), pp 1–13. doi: 10.1093/biomet/87.1.1

[24] Toal, D.J.J. and Keane, A.J. Efficient multipoint aerodynamic design optimization via cokriging, *J. Aircr.*, 2011, **48**, (5), pp 1685–1695. doi: 10.2514/1.C031342

[25] Priyanka, R., Sivapragasam, M. and Narahari, H.K. Multi-fidelity aerodynamic optimization of an airfoil at a transitional low Reynolds number, *Lecture Notes Mech. Eng.*, 2021. doi: 10.1007/978-981-15-9601-8_18

[26] Tejero, F., MacManus, D. and Hueso-Rebassa, J. Aerodynamic optimisation of civil aero-engine nacelles by dimensionality reduction and multi-fidelity techniques, *Int. J. Numer. Methods Heat Fluid Flow*, 2022. doi: 10.1108/hff-06-2022-0368

[27] Shi, R., Long, T. and Baoyin, H. Multi-fidelity and multi-objective optimization of low-thrust transfers with control strategy for all-electric geostationary satellites, *Acta Astronaut.*, 2020, **177**, pp 577–587. doi: 10.1016/j.actaastro.2020.08.013

[28] Qian, P.Z.G. Nested Latin hypercube designs, *Biometrika*, 2009, **94**, (4), pp 957–970. doi: 10.1093/biomet/asp045

[29] Deb, K., Pratap, A., Agarwal, S. and Meyarivan, T. A fast and elitist multiobjective genetic algorithm: NSGA-II, *IEEE Trans. Evol. Comput.*, 2002, **6**, (2), pp 182–197. doi: 10.1109/4235.996017

[30] Kulfan, B. and Bussoletti, J. "Fundamental" parameteric geometry representations for aircraft component shapes, In 11th AIAA/ISSMO *M*ultidisciplinary *A*nalysis and *O*ptimization *C*onference, 2006, p. 6948. doi: 10.2514/6.2006-6948

[31] Kulfan, B.M. Universal parametric geometry representation method, *J. Aircr.*, 2008, **45**, (1), pp 142–158. doi: 10.2514/1.29958

[32] Zhu, F. and Qin, N. Intuitive class/shape function parameterization for airfoils, *AIAA J.*, 2014, **52**, (1), pp 17–25. doi: 10.2514/1.J052610

[33] Christie, R., Heidebrecht, A. and MacManus, D. An automated approach to nacelle parameterization using intuitive class shape transformation curves, *J. Eng. Gas Turbines Power*, 2017, **139**, (6), pp 1–9. doi: 10.1115/1.4035283

[34] Goulos, I., Stankowski, T. and Otter, J. Aerodynamic design of separate-jet exhausts for future civil aero-engines – Part I: parametric geometry definition and computational fluid dynamics approach, *J. Eng. Gas Turbines Power*, 2016, **138**, (8), pp 1–14. doi: 10.1115/1.4032649

[35] Diskin, B., Anderson, W.K. and Pandya, M.J. *Grid convergence for three dimensional benchmark turbulent flows, In 2018 AIAA Aerospace Sciences Meeting,* 2018, p. 1102. doi: 10.2514/6.2018-1102

[36] Re, R.J. and Abeyounis, W.K. A wind tunnel investigation of three NACA 1-series inlets at mach numbers up to 0.92, *J. Eng. Gas Turbines Power*, 1996. https://ntrs.nasa.gov/citations/19970010380

[37] Anderson, W.K. and Bonhaus, D.L. An implicit upwind algorithm for computing turbulent flows on unstructured grids, *Comput. Fluids*, 1994, **23**, (1), pp 1–21. doi: 10.1016/0045-7930(94)90023-X

[38] Anderson, W.K., Rausch, R.D. and Bonhaus, D.L. Implicit/multigrid algorithms for incompressible turbulent flows on unstructured grids, *J. Comput. Phys.*, 1996, **128**, (2), pp 391–408. doi: 10.1006/jcph.1996.0219

[39] Nielsen, E.J. Aerodynamic Design Sensitivities on an Unstructured Mesh Using the Navier-Stokes Equations and a Discrete Adjoint Formulation: Virginia Polytechnic Institute and State University, 1998. http://hdl.handle.net/10919/29459

[40] Magrini, A. and Benini, E. Study of geometric parameters for the design of short intakes with fan modelling, *Chin. J. Aeronaut.*, 2022, **35**, (11), pp 18–32. doi: 10.1016/j.cja.2022.01.018

[41] Sobester, A., Forrester, A. and Keane, A. *Engineering Design via Surrogate Modelling: A Practical Guide*: John Wiley & Sons, 2008. doi: 10.1002/9780470770801

[42] Bouhlel, M.A., Hwang, J.T. and Bartoli, N. A Python surrogate modeling framework with derivatives, *Adv. Eng. Softw.*, 2019, **135**, 102662. doi: 10.1016/j.advengsoft.2019.03.005

[43] Kitayama, S., Srirat, J., Arakawa, M. and Yamazaki, K. Sequential approximate multi-objective optimization using radial basis function network, *Struct. Multidiscip. Optim.*, 2013, **48**, (3), pp 501–515. doi: 10.1007/s00158-013-0911-z

[44] Zitzler, E. and Thiele, L. Multiobjective evolutionary algorithms: a comparative case study and the strength Pareto approach, *IEEE Trans. Evol. Comput.*, 1999, **3**, (4), pp 257–271. doi: 10.1109/4235.797969

[45] Czyz, P. and Jaszkiewicz, A. Pareto simulated annealing—a metaheuristic technique for multiple-objective combinatorial optimization, *J. Multi-Criteria Decisi. Anal.*, 1998, pp 34–47.

[46] Huband, S., Hingston, P., Barone, L. and While, L. A review of multiobjective test problems and a scalable test problem toolkit, *IEEE Trans. Evol. Comput.*, 2006, **10**, (5), pp 477–506. doi: 10.1109/TEVC.2005.861417

[47] Christie, R., Ramirez, S. and MacManus, D.G. Aero-engine installation modelling and the impact on overall flight performance, In Advanced *A*ero *C*oncepts, *D*esign and *O*perations *C*onference, Bristol, 2014. https://www.researchgate.net/publication/341354251_Aero-engine_installation_modelling_and_the_impact_on_overall_flight_performance